

X-ray spectral studies of TeV γ -ray emitting blazars

Alicja Wierzcholska^{1,2*}, Stefan J. Wagner¹

¹Landessternwarte, Universität Heidelberg, Königstuhl 12, D 69117 Heidelberg, Germany

²Institute of Nuclear Physics, Polish Academy of Sciences, ul. Radzikowskiego 152, 31-342 Kraków, Poland

Accepted Received ...; in original form ...

ABSTRACT

This work is a summary of the X-ray spectral studies of 29 TeV γ -ray emitting blazars observed with *Swift*/XRT especially focusing on sources for which X-ray regime allows to study the low and the high energy ends of the particle distributions function. Variability studies require simultaneous coverage, ideally sampling different flux states of each source. This is achieved using X-ray observations by disentangling the high-energy end of the synchrotron emission and the low-energy end of the Compton emission, which are produced by the same electron population. We focused on a sample of 29 TeV γ -ray emitting blazars with the best signal-to-noise X-ray observations collected with *Swift*/XRT in the energy range of 0.3-10 keV during 10 years of *Swift*/XRT operations.

We investigate the X-ray spectral shapes and the effects of different corrections for neutral hydrogen absorption and decompose the synchrotron and inverse Compton components. In the case of 5 sources (3C 66A, S5 0716+714, W Comae, 4C +21.35 and BL Lacertae) a superposition of both components is observed in the X-ray band, permitting simultaneous, time resolved studies of both ends of the electron distribution. The analysis of multi-epoch observations revealed that the break energy of X-ray spectrum varies only by a small factor with flux changes. Flux variability is more pronounced in the synchrotron domain (high-energy end of the electron distribution) than in the Compton domain (low energy end of the electron distribution). The spectral shape of the Compton domain is stable, while the flux of the synchrotron domain is variable. These changes cannot be described by simple variations of the cut-off energy, suggesting that the high-energy end of the electron distribution is not generally well-described by cooling only.

Key words: Radiation mechanisms: non-thermal — Galaxies: active — BL Lacertae objects: general — Galaxies: jets

1 INTRODUCTION

BL Lacertae (BL Lac) type objects as well as Flat Spectrum Radio Quasars (FSRQ) constitute a class of Active Galactic Nuclei (AGN). In a unified model, these are the sources characterized by polarized and highly variable non-thermal continuum emission observed from the jet pointing at small angles to the line of sight (e.g., Begelman et al. 1984). The radiation observed extends from radio wavelengths up to the X-ray regime, or even - in the case of the most energetic sources - up to high and very high energy γ -ray range (e.g. Wagner 2009; Vercellone et al. 2011; H.E.S.S. Collaboration 2013c, 2014). The emission observed from blazars is known to be variable at all wavelengths on different timescales down to hours or even minutes in the

most extreme cases (e.g. Wagner & Witzel 1995; Aharonian et al. 2007c; Gopal-Krishna et al. 2011; Saito et al. 2013; Liao & Bai 2015). Also, flux changes in blazars are often associated with spectral variability (e.g. Xue et al. 2006; Böttcher et al. 2010; Gaur 2014).

The spectral energy distribution (SED), in ν - νF_ν representation, shows in most cases two broad emission components. The low energy peak is usually attributed to synchrotron radiation of relativistic electrons from the jet, while the origin of the high-energy peak still remains matter of debate. In the most common leptonic scenarios, the high-energy bump is explained as inverse Compton radiation from the same population of relativistic electrons scattering either the synchrotron photons (SSC, Synchrotron Self Compton models; e.g. Maraschi et al. 1992; Kirk et al. 1998) or external photons from the surroundings, e.g. accretion disc, broad lines region or dust (EC, External Compton

* E-mail: alicja.wierzcholska@ifj.edu.pl

models: e.g. Dermer et al. 1992; Sikora et al. 1994). Alternatively, the high-energy peak can be explained in the framework of hadronic scenarios. In this case the high-energy radiation is produced in processes such a proton synchrotron emission, synchrotron and Compton emission from secondary decay products of charged pions, or π_0 decay (Aharonian 2000; Atoyan & Dermer 2003; Mücke et al. 2003; Böttcher et al. 2013). Additionally, Petropoulou & Mastichiadis (2015) have shown that Bethe-Heitler emission can explain SED of blazars in the case when the typical double-humped structure is not clearly visible.

Depending on the frequency of the low-energy peak, BL Lac type blazars can be subdivided into high-, intermediate- and low-energy peaked objects: HBL, IBL, LBL, respectively (see, e.g., Padovani & Giommi 1995; Fossati et al. 1998; Abdo et al. 2010). For LBL type blazars the synchrotron peak is located in the infrared regime ($\nu_s \leq 10^{14}$ Hz), for IBL blazars in the optical-UV range (10^{14} Hz $< \nu_s \leq 10^{15}$ Hz), while for HBL blazars in the X-ray domain ($\nu_s > 10^{15}$ Hz) (Abdo et al. 2010). It has been proposed and connected with decreasing bolometric luminosities and γ -ray dominance by Fossati et al. (1998). According to the blazar sequence, HBL blazars are synchrotron dominated, while FSRQs are γ -ray dominated. In the later work the concept of the blazars sequence has been updated with a large sample of radio-loud AGNs to the blazars envelope (Meyer et al. 2011).

The different classes of blazars could also be distinguished according to the location of the X-ray spectrum in SED. For HBL type blazars the X-ray spectrum is usually located in the synchrotron domain. While in the case of IBL type sources the X-ray emission usually covers both synchrotron and inverse Compton component. For several IBL type sources the upturn of SED located in the X-ray domain has been reported e.g. BL Lacertae (Tanihata et al. 2000; Ravasio et al. 2002; Donato et al. 2005), W Comae (Tagliaferri et al. 2000; Donato et al. 2005), S5 0716+71 (Cappi et al. 1994; Giommi et al. 1999; Tagliaferri et al. 2003; Donato et al. 2005; Ferrero et al. 2006; Wierzcholska & Siejkowski 2015), AO 0235+16 (Raiteri et al. 2006), OQ 5310 (Tagliaferri et al. 2003), 3C 66A (Donato et al. 2005). LBL type objects are usually characterised with the X-ray spectrum covering the inverse Compton bump.

The X-ray observations of the brightest HBL type blazars unfolded strong variability often with large amplitude of variations, observed on long as well as on short timescales (Sembay et al. 1993; Tanihata et al. 2000; Sembay et al. 2002; Zhang et al. 2002, 2005). In several mentioned cases HBLs variability amplitudes have been also found to be correlated with the energy. Furthermore, HBL blazars are known for “harder-when-brighter” behaviour manifested in hardening of spectral index with the increasing flux level observed (e.g. Pian et al. 1998; Zhang et al. 2005, 2006; H.E.S.S. Collaboration 2012).

The X-ray variability studied in different energy bands seem to be correlated, often with time-lags of a few hours. Usually variations observed in lower energies have lags behind those at higher energies (so-called soft time-lags), but the opposite (so-called hard time-lags) are also observed (e.g. Zhang et al. 2006; Fossati et al. 2000). Furthermore, the comparison of X-ray spectral index (α) and flux intensity (I) presented in a α -I plots reveals clockwise (for soft time-lags) or counter-clockwise (for hard time-lags) patterns

(e.g. Takahashi et al. 1996; Ravasio et al. 2004; Brinkmann et al. 2005). The time-lags are directly related with changes of acceleration and cooling time scales (Kirk et al. 1998).

The X-ray variability observed in the case of IBL and LBL type objects show similar behaviour according to the variability time scales and amplitudes observed for HBL type blazars. But, for these classes of blazars, as opposed to HBL type ones, the variability amplitudes seem to be anticorrelated with the emission energy (e.g. Giommi et al. 1999; Ravasio et al. 2002). Furthermore, in mentioned studies no time-lags between the low and the high energy X-ray emission has been observed.

Previous studies focusing on the nature of the X-ray spectra disclosed its complex nature and several authors discussed features of blazars behaviour in this domain. Worrall & Wilkes (1990) analysed large sample of BL Lac type blazars observed with *Einstein* which were well described with the single power-law model with a wide range of spectral indices. This model as well as the broken power-law one were also successfully used to describe the X-ray spectra in the later works for data collected with different instruments like ASCA (e.g. Kubo et al. 1998), *BeppoSAX* (e.g. Wolter et al. 1998; Padovani et al. 2001, 2004), HEAO-1 (e.g. Sambruna et al. 1994) and ROSAT observations (e.g. Perlman et al. 1996; Urry et al. 1996; Sambruna et al. 1996).

Alternatively, in a several works the X-ray spectra are well described with the curved log-parabola model. Inoue & Takahara (1996); Tavecchio et al. (1998); Giommi et al. (2002); Donato et al. (2005) studied the X-ray observations of blazars performed with *BeppoSAX* and found this model as preferable for at least 50% of the sources analysed. In the later studies Massaro et al. (2004a,b, 2006) analysed the X-ray spectra for Mrk 421 and Mrk 501 and found the log-parabola as the best model for characterization of their spectra in different activity states. The authors also suggested a possible interpretation of the mentioned model in term of statistical particle acceleration with the assumption that the probability of the increase of particles energy is a decreasing function of an energy. Furthermore Massaro et al. (2008) enlarged their sample to 15 objects and found the log-parabola as the best model for most of the blazars spectra studied.

The mentioned studies revealed that the X-ray spectra are characterized with a wide range of spectral indices. Following the distributions presented by Donato et al. (2005), which are consistent with the previous and the later studies by e.g. Perlman et al. (2005); Tramacere et al. (2007); Massaro et al. (2008), the X-ray spectral indices of HBL type blazars are between $\Gamma_X = 1.8$ and $\Gamma_X = 3.0$, for LBL type objects this quantity is between $\Gamma_X = 1.5$ and $\Gamma_X = 1.8$, while in the case of FSRQs, spectra are best described with the spectral indices between $\Gamma_X = 1.0$ and $\Gamma_X = 2.0$.

The motivation of this work is to test if the X-ray spectra observed with *Swift*/XRT in the energy range of 0.3-10 keV are well described with the single power-law model or the continuously curved log-parabola. Both characteristics are reasonable and widely discussed in the context of models used for description of synchrotron ageing and acceleration processes (e.g. Leahy 1991; Massaro et al. 2004a,b). Also, we would like to check for how many of selected TeV emitting blazar the X-ray regime is a place, where the low- and the high-energy spectral component meet or if the X-

ray spectral shape allows us to predict where this point for particular blazars is located in broadband SED. Finally, different values of the Galactic column absorption provided in several surveys (Dickey & Lockman 1990; Kalberla et al. 2005; Willingale et al. 2013) give us reason to study, which values are preferable and how changes in the Galactic column density values influence the X-ray spectral properties.

The paper is organized as follows: the Swift Gamma-Ray Burst Mission is described in Sect. 2, while Sect. 3 gives information about the sample selection and data analysis. All selected sources are described in Sect. 4. Sect. 5 focusses on 5 blazars, for which an upturn point is visible in the X-ray regime. The work is summarized in Sect. 6.

2 THE SWIFT GAMMA-RAY BURST MISSION

The Swift Gamma-Ray Burst Mission (hereafter *Swift*) (Gehrels et al. 2004), launched in November 2004, is a multi-wavelength space observatory, equipped with three instruments: the Burst Alert Telescope (BAT, Barthelmy et al. 2005), the X-ray Telescope (XRT, Burrows et al. 2005) and the Ultraviolet/Optical Telescope (UVOT, Roming et al. 2005). *Swift*/XRT operates in the energy range of 0.3-10 keV.

The XRT detector can be operated in different modes: the Windowed Timing (WT), the Photon Counting (PC) and the Imaging (IM); the forth - Photo-Diode mode - is not working since May 2005. In the PC mode the full CCD chip is read out every 2.5 seconds and it is used for sources with count rate smaller than 1 count per second. Observations provided in this mode have full imaging and spectroscopic resolution. The WT mode is characterized by 1.7 ms time resolution and full energy resolution. The mode is usually used to observe the sources with count rate larger than 1 count per second. During the monitoring of a chosen source, the detector can switch between the PC and the WT mode, to optimize the observations. The third, Imaging mode is used only to obtain the first X-ray position of a newly detected Gamma Ray Burst.

3 SAMPLE SELECTION AND DATA ANALYSIS

The catalogue of TeV sources (TeVcat¹) includes 161² objects and 58 of them are classified as blazars. All of the blazars were observed several times with *Swift*/XRT. The main properties of the TeV blazars, as well as the total exposure in the PC mode and integrated flux for the energy range of 0.3-10 keV obtained using the online analysis of *Swift*/XRT data (Evans et al. 2009) are collected in Table 1. Since the aim of this work is to focus on properties of the average X-ray spectra for particular blazars, the further analysis has been limited to objects with the best *Swift*/XRT data for which the product of the integrated flux and the exposure is greater than $3.0 \cdot 10^{-10}$ erg cm⁻².

This allowed to single out 29 objects with high signal-to-noise level, and for which *Swift*/XRT data allow to obtain good-quality spectra. The sources chosen are marked in the last column in Table 1. One object, namely, IC 310, fulfilled our criteria but it is not included in our sample, since in the literature it is not classified as a blazar, but as a radio-galaxy or a transition object between radio galaxy and BL Lac type source (e.g. Kadler et al. 2012; Aleksić et al. 2014d).

This study is limited to observations taken in the PC mode, since data taken in the WT mode are affected by charge redistribution problems inherently related to the way in which the CCD of the instrument is read. These depend on the position of the source on the CCD before binning the read out on a 10 pixel basis and makes the response position-dependent. The effect is small for mildly absorbed sources, but in this study we focus on long time integrated spectra, so a number of photons is huge and it can be seen as an impact on the residuals in spectra.³ The effect was also noticed in *Swift*/XRT observation in WT mode by e.g. Massaro et al. (2008).

For 29 selected blazars *Swift*/XRT data were analysed using HEASoft package v. 6.16 software⁴ with CALDB v. 20140120. All events are cleaned and calibrated using the `xrtpipeline` task. Data in the energy range of 0.3-10 keV with grades 0-12 are analysed. For the spectral studies, data are grouped using the `grappa` tool to have a minimum 20 counts per bin and the co-added spectra are fitted using XSPEC v. 12.8.2 (Arnaud 1996).

In the first step two models were used to fit *Swift*/XRT spectrum:

- a single power-law defined as

$$\frac{dN}{dE} = N_p \left(\frac{E}{E_0} \right)^{-\Gamma}, \quad (1)$$

with the Galactic absorption,

- a logarithmic parabola defined as

$$\frac{dN}{dE} = N_l \left(\frac{E}{E_0} \right)^{-(\alpha + \beta \log(E/E_0))}, \quad (2)$$

with the Galactic absorption.

Here, the power-law model is characterized by the normalization N_p and the spectral index Γ (at energy E_0), while the log-parabola model is described with the normalization N_l and the curvature parameter β and the spectral index α (at energy E_0). In both cases the scale energy E_0 is fixed at 1 keV. In each case four different values of the Galactic absorption parameter are tested:

- N_H^{LAB} taken from the Leiden Argentine Bonn Survey (LAB, Kalberla et al. 2005). The survey gives an information about N_H^{LAB} values for different region of the sky. The map was obtained by merging two surveys: the Leiden/Dwingeloo Survey (Hartmann & Burton 1997) and Instituto Argentino de Radioastronomia Survey (Arnal et al. 2000; Bajaja et al. 2005). The beamsize is 36 *arcmin* for declinations > -27.5 deg and 30 *arcmin* for declinations < -27.5 deg. The uncertainties are in each case at a 2-3% level.

¹ <http://tevcats.uchicago.edu/>

² The number of objects collected in catalogue up to June 2015.

³ Private communication by Sergio Campana.

⁴ <http://heasarc.gsfc.nasa.gov/docs/software/lheasoft>

- N_H^{DL} taken from the survey by (Dickey & Lockman 1990) (hereafter DL). The map was obtained by merging several surveys and averaging into 1×1 degree bins.

- N_H^{Will} taken from the survey by Willingale et al. (2013) (hereafter Will). The survey gives values of $N_{H,tot}$, which includes both the atomic gas column density N_{HI} and the molecular hydrogen column density N_{H_2} . N_{HI} is taken from LAB survey, while N_{H_2} is estimated using the maps of dust infrared emission by Schlegel et al. (1998) and the dust-gas ratio by Dame et al. (2001).

- free N_H^{free} value.

All N_H values are collected in Table 2 (in the online material). Additionally, in the case when the log-parabola model is the preferable one and β in this model is consistently negative for all N_H values tested the spectrum is also fitted with the broken power-law model (also with the Galactic absorption) described as:

$$\frac{dN}{dE} = N_b \times \begin{cases} (E/E_b)^{-\Gamma_1} & \text{if } E < E_b, \\ (E/E_b)^{-\Gamma_2} & \text{otherwise.} \end{cases} \quad (3)$$

This model is characterized by normalization N_b , two spectral indices Γ_1 and Γ_2 , and the break energy E_b . It allows to determine the value of the break energy, E_b , the exact point at which spectrum is broken. This parameter is important in the case of blazars for which the X-ray spectrum covers both synchrotron and inverse Compton components. Since BL Lacertae is known to have a spectral upturn located in the X-ray domain (e.g. Tanihata et al. 2000; Rivasio et al. 2002), we also decided to fit the spectrum of this blazars with the broken power-law model.

For all the models mentioned the fitting method in XSPEC is set to `leven`, a minimization method using the modified Levenberg-Marquardt algorithm (Marquardt 1963; Bevington & Robinson 2003).

4 THE *Swift*/XRT SPECTRAL CATALOGUE

Following the procedure described in Sect. 3 for 29 selected objects *Swift*/XRT spectra has been fitted with log-parabola and power-law models. The fit parameters for the log-parabola and the power-law fits are collected in Table 3 and Table 4 (in the online material), respectively. Since the log-parabola and the power-law are nested models, the goodness of both fitted models is compared using the F-test (e.g. Bevington & Robinson 2003). The test statistics value as well as the corresponding probability are collected in Table 4 (in the online material). For the additional analysis with the broken power-law model the spectral fit parameters are collected in Table 5 (in the online material).

Spectral fits for the log-parabola and the power-law models are presented in Fig. 6 and Fig. 2 (in the online material). Both figures presents data points fitted with N_H value from the LAB survey. Four models are presented for each blazar with colours denoting four different N_H values: red is used for the N_H value taken from Kalberla et al. (2005) survey, blue for the one from Dickey & Lockman (1990), magenta for the N_H value from Willingale et al. (2013) and green for the free N_H value. Figures 3–7 (in the online material) show spectra for all selected 29 objects and data shown in the figures are always fitted with the log-parabola model with the N_H value taken from the LAB survey.

Different models and N_H values tested lead to the conclusion that in the most cases of TeV γ -ray emitting blazars studied the preferable description of the X-ray spectrum is the log-parabola model. Only in the cases 1ES 1101-232, Mrk 180 and PKS 2005-489, the F-test values imply that the average spectrum is best fitted with a single power-law model.

The preferable fits do not allow us to distinguish a best, universal N_H value, which could be used in all cases. In the sample of 29 sources we found that the values taken from LAB, Willingale et al. (2013), Dickey & Lockman (1990) are preferable in 6, 8, 5 sources, respectively, while in the other 10 cases, a free N_H value provides the best χ_{red}^2 result. The selection of the preferable model and N_H value was based not only on the fit to the X-ray data characterised with χ_{red}^2 , but also in divergent cases we investigate the shape of the fitted spectrum in the context of the overall broadband spectral energy distribution built from archival data⁵. In the sample studied there are a few objects (such like PKS 0548-322, H 1426+428 or PKS 2155-304) for which different N_H value result in a very similar X-ray spectral curvature. But there are also several cases for which different surveys provide different Galactic column density values, which result in very different spectral curvatures. An extreme example is 1ES 0033+595 (see in Fig. 6). In several cases spectra with very different characterisations are fitted with very similar values of χ_{red}^2 .

In our collection of 29 X-ray spectra we found that the shape of spectra is characterised with α or Γ (depending on the preferred model of the spectrum) in the range 1.3-2.6. For the fit with a log-parabola model the curvature parameter β lies between -0.100 and -0.347 for the concave curved spectra and between 0.066 and 0.477 for the convex curved spectra. Below, main properties of the X-ray spectra for the selected 29 objects in the context of our and previous studies are discussed:

4.1 Notes on individual objects

1ES 0033+595: The X-ray spectrum of this blazar is well described with the log-parabola model ($\chi_{red}^2 \sim 1.0$). The power-law fits result in $\chi_{red}^2 \sim 1.8$ and it is less favoured. Comparing different values of the Galactic column density, we conclude that the best fit to data is obtained using fixed N_H value provided by Willingale et al. (2013) or with free N_H value. A low value of N_H , e.g. from Kalberla et al. (2005) or Dickey & Lockman (1990), causes an artificial bump in the synchrotron component in SED. 1ES 0033+595 is an extreme example of a source for which different N_H values used result in significant changes in the spectral shapes, while χ_{red}^2 values differ only slightly.

Previous studies of the X-ray observations of 1ES 0033+595 with *BeppoSAX* by Giommi et al. (2002) also favour the log-parabola model for the description of the X-ray spectrum, with $\alpha = 1.4$ and $\beta = 0.4$. These results are consistent with the ones obtained in this paper in the case of log-parabola fit with N_H value taken from Willingale et al. (2013). Donato et al. (2005) claimed a power-law as a good model for later *BeppoSAX* observations with spectral

⁵ <http://www.asdc.asi.it/>

index of $\Gamma = 2.1$ and free N_H value significantly smaller than N_H values from discussed surveys.

RGB J0136+391: The X-ray spectrum of the blazar is well characterized with the log-parabola model with all N_H values tested or with the power-law with free N_H value and the one provided by Willingale et al. (2013). The preferable fits result in χ_{red}^2 of about 0.9, while in the latter case χ_{red}^2 is about 1.3. Donato et al. (2001) found single power-law with free N_H value as the favourable model for this source.

3C 66A: The X-ray spectrum for the blazar is best described with the log-parabola model ($\chi_{red}^2 \sim 0.95$). For the comparison the power-law model fitted to data result in $\chi_{red}^2 \sim 1.1-1.2$. Negative values of the β parameter in all log-parabola fits confirm the concave curvature of the fitted model and indicate that the turning point of SED is located in the *Swift*/XRT energy range. We found the break energy value of (3.4 ± 0.3) keV by fitting also the broken power-law model to data. We also found N_H value from Kalberla et al. (2005) as the best one for the blazar. The log-parabola fit with free value of N_H results in parameter value significantly smaller than the ones provided by the surveys considered.

In the previous studies Donato et al. (2005) found power-law with free N_H value or curved power-law as preferable description of X-ray spectrum. We note that in the latter case the curvature is not significant. The spectral indices mentioned by the authors ($\Gamma = 2.2-2.4$) is about 5% smaller than results presented in this paper.

1ES 0229+200: In the case of this blazar the comparison of the log-parabola and the power-law fits slightly favours description of the spectrum in the X-ray domain with the first ones. The log-parabola model result in $\chi_{red}^2 \sim 1.16$, while the power-law one results in $\chi_{red}^2 \sim 1.20-1.38$. Regarding the different values of the Galactic column density tested, the value taken from Kalberla et al. (2005) survey is preferred.

In the previous studies the curvature of the spectrum in the X-ray domain was also suggested by Massaro et al. (2008) for observations obtained with *BeppoSAX*, XMM-Newton and *Swift*/XRT. The results obtained by authors are consistent with results from this paper with N_H value from Willingale et al. (2013) survey. Donato et al. (2005) analysed the *BeppoSAX* observations of the blazar and found the power-law model with free N_H value as the best one for this source. The spectral index obtained by Donato et al. (2005) is $\Gamma = 2.0$, and it is significantly larger than values from this paper.

PKS 0447–439: The spectrum in the X-ray range for this source is well described with the log-parabola model with $\chi_{red}^2 \sim 1.1$. For the comparison the power-law model fitted to data results in $\chi_{red}^2 \sim 1.2-1.4$. With different values of N_H tested the one provided by Dickey & Lockman (1990) is found as the best one.

In the previous studies of the X-ray data collected with *Swift*/XRT H.E.S.S. Collaboration (2013b) described the blazar spectrum with the power-law model with the spectral index $\Gamma = 2.8-3.3$. The authors did not find any significant improvement when using the broken power-law model.

1ES 0502+675: The X-ray spectrum for this blazar can be equally well characterized using either the power-law fit or the log-parabola one. For the case of the power-law model satisfying fit parameters are obtained using free N_H value or the one provided by Willingale et al. (2013), and in both cases $\chi_{red}^2 \sim 1.0-1.1$. For the log-parabola fit also the same N_H gives the best $\chi_{red}^2 \sim 1.0$ values. For the case of the log-parabola model fitted with N_H values provided by Kalberla et al. (2005) and Dickey & Lockman (1990) we got also acceptable fits with $\chi_{red}^2 \sim 1.1$. Different amounts of N_H are compensated by different degrees of curvature β .

No need for curved model for the description of the *BeppoSAX* observations was found by Donato et al. (2005). The authors favour the single power-law description of the X-ray spectrum, with the spectral index of 2.3. This value is similar to the one from our study for the case free N_H value.

PKS 0548–322: The spectrum is well described with both a log-parabola and a power-law model. For the log-parabola model we do not find any preferable value of N_H . In each case the spectral fits result in very similar values of the spectral parameters and a χ_{red}^2 of about 1.0. In the case of the power-law fit with a free N_H value or the one taken for Willingale et al. (2013). Fits give a χ_{red}^2 of about 1.0-1.1.

Donato et al. (2005) found that both a power-law and a log-parabola can characterize the X-ray spectrum with the spectral indices of about 2.3-2.4. Giommi et al. (2002) prefer the log-parabola model for *BeppoSAX* observations with spectral index of 1.5 and the curvature parameter 0.5. For the comparison in this paper the preferable spectral index is 1.7 and the curvature parameter about 0.2.

The studies of several *BeppoSAX*, XMM-Newton and *Swift*/XRT observations of the source performed by Massaro et al. (2008) confirmed that the X-ray spectrum has a curved log-parabolic shape. Also, Aharonian et al. (2010) found the broken power-law model with spectral indices of 1.7 and 2.0 and the break energy of 1.7 keV as better than the power-law one for the case of *Swift*/XRT observations of the blazar.

1ES 0647+250: The source is well described with the log-parabola model. Different values of N_H results in similar χ_{red}^2 value of about 1.1, while in the case of the power-law model χ_{red}^2 is in the range of 1.2-2.0, depending on N_H value used. 1ES 0647+250 is an example of a blazar, for which in the case of the log-parabola fit very similar χ_{red}^2 values for different N_H tested reveal significantly different curvatures with β in the range from 0.17 up to 0.45.

S5 0716+714: The *Swift*/XRT spectrum is well described by a log-parabola model with χ_{red}^2 of about 1.0. For the comparison the single power-law model tested gives χ_{red}^2 of about 1.2. Different values of N_H in the case of the log-parabola fit show slightly similar concave curvature with β of about (-0.22) - (-0.15) . Also the broken power-law one gives a reasonable fit with χ_{red}^2 of 1.2. In this case the break energy is found as $E_b = (1.10 \pm 0.10)$ keV.

The curvature of the spectrum in the X-ray domain has been suggested in several studies. Tagliaferri et al. (2003), Ferrero et al. (2006) and Donato et al. (2005) found a broken power-law model as the preferable one with energy break of 1.5 keV, 1.5-5.3 keV and 1.75-2.73 keV respectively.

1ES 0806+524: The best characterisation of the shape of the X-ray spectrum for this blazar is given using either the log-parabola fit, with any of tested N_H values, or with the power-law model, with a free N_H value. For all the log-parabola fits and the single power-law with free N_H , χ_{red}^2 is around 1.0. Previous studies focusing on the *Swift*/XRT observations of 1ES 0806+524 did not reveal a need for a curved model (Acciari et al. 2009). The authors describe source with the power-law model with spectral index of 2.5-2.7, which is consistent with the results from this paper.

1ES 1011+496: The spectrum of 1ES 1011+496 can be well characterized using the log-parabola model with any of considered N_H values. The models fitted result in χ_{red}^2 of about 0.9-1.0. For the single power-law model χ_{red}^2 is in the range of 1.3 and 1.6, depending on N_H value chosen. The previous studies of the *Swift*/XRT observations by Reinthal et al. (2012) show data that are well fitted with the power-law model.

1ES 1101–232: The X-ray spectrum is well described using the power-law as well as the log-parabola models, in both cases with any of N_H values tested. In all cases χ_{red}^2 for each of the N_H value tested is about 1.0. In the case of this blazar values of N_H taken from different surveys result in very similar fit parameters (α , β , Γ).

Donato et al. (2005) found a log-parabola as the preferred model for the X-ray spectrum obtained using *BeppoSAX* observations. Also Massaro et al. (2008) favour the curved model, characterized with $\alpha = 1.6-1.9$ and $\beta = 0.3$.

Mrk 180: All spectral fits with a log-parabola model with any of N_H values tested here result in reasonable χ_{red}^2 value. A good fit to data is obtained with a power-law model, but only with free N_H value ($\chi_{red}^2 \sim 1.0$). The previous observation of the source obtained with *BeppoSAX* are well described with the log-parabola model with $\alpha = 2.1$ and $\beta = 0.4$. (Giommi et al. 2002).

RX J1136.5+6737: The power-law model is a good description of the X-ray spectrum of this blazar ($\chi_{red}^2 \sim 1.0$). This spectrum is also well characterized with the log-parabola model. In the first case χ_{red}^2 is about 1.0, while in the latter 1.1. No preferable N_H value has been found for this source either in the case of single power-law model fitted or the log-parabola one.

1ES 1218+304: The log-parabola model result in similar values of $\chi_{red}^2 \sim 1.2$ for the different values of N_H tested. Also, in the case of the power-law different values of N_H tested give comparable results $\chi_{red}^2 \sim 1.3$. In both cases, the curvature and the spectral parameters of the fits do not differ significantly.

The log-parabola model is the favourable one for the spectrum characterization for *BeppoSAX* (Donato et al. 2005; Massaro et al. 2008), XMM-Newton (Massaro et al. 2008) and *Swift*/XRT observations (Tramacere et al. 2007; Massaro et al. 2008). Furthermore Giommi et al. (2002) found that *BeppoSAX* observations in the X-ray range can be well described with a sum of two power-law models.

W Comae: The log-parabola model is a more plausible scenario for the X-ray spectrum characterization (χ_{red}^2 of about 1.0). Since W Comae is fitted with concave curvature, in order to find the break energy for this source, we also fitted the X-ray observations using the broken power-law model. We found $E_b = (2.01 \pm 0.22)$ keV. In the case of the log-parabola model fitted the comparison of different N_H values favours the N_H value taken from Willingale et al. (2013) survey.

In previous studies the curvature of the spectrum obtained with *BeppoSAX* observations was also preferred by Tagliaferri et al. (2000) and Donato et al. (2005). Donato et al. (2005) claim that the break energy is equal to $E_b = 3.09_{-1.38}^{+1.03}$ keV or $E_b = 2.70_{-1.33}^{+0.47}$ keV. Tagliaferri et al. (2000) has found similar values of E_b .

MS 1221.8+2452 The blazar in the X-ray regime is described with the log-parabola model with any of N_H values tested and with the power-law model with free value of the Galactic absorption column density. For the other cases χ_{red}^2 is about 1.5, while for the preferable cases $\chi_{red}^2 \sim 1.1$.

4C +21.35: Power-law and log-parabola fits result in χ_{red}^2 of about 1.0 and ~ 1.7 , respectively.

Negative values of a β parameter in the case of the log-parabola model imply an up-turn of SED located in the X-ray range. The broken power-law fit to data placed the break energy at (1.18 ± 0.10) keV. The best description of the log-parabola fits is given with free N_H value, but this is much smaller than the ones provided by Kalberla et al. (2005), Dickey & Lockman (1990) or Willingale et al. (2013). The latter discussed values of N_H describe the spectrum with a comparable accuracy.

3C 279: The X-ray spectrum is well explained using the log-parabola model and different values of N_H result in consistent $\chi_{red}^2 \sim 1.1$. The power-law model can also be used for this source, but only with free N_H value. Fits with the Galactic absorption values taken from the surveys results in $\chi_{red}^2 \sim 1.3$. For the log-parabola model different values of N_H tested result in very similar values of α and β parameters.

In the previous studies Donato et al. (2005) found that *BeppoSAX* observations of 3C 279 can be characterised with the power-law and the broken power-law models, depending on the observation date. In the latter case the break energy point is in low energies $\sim 0.5-0.7$ keV.

PKS 1424+240: In the energy range of 0.3-10 keV the spectrum can be well characterized with the log-parabola model with all N_H values tested and with the power-law model, but only with free N_H value. In all the mentioned cases the spectral fitting results in $\chi_{red}^2 \sim 1.0$. For the comparison the other power-law fits, with N_H values provided by Kalberla et al. (2005), Dickey & Lockman (1990) or Willingale et al. (2013) result in χ_{red}^2 of about 1.4-1.5. Acciari et al. (2010a) found single power-law model as preferable to describe X-ray spectrum of the blazar. Similar result found Aleksić et al. (2014a) for the *Swift*/XRT observations of PKS 1424+240.

H 1426+428: A log-parabola model provides χ_{red}^2 value of about 1.2, while in the case of the power-law model the fitted χ_{red}^2 is about 1.6-1.7. All N_H values tested in the case of the

log-parabola model give comparable results regarding the spectral index and the curvature parameter.

The curved shape of the spectrum of the blazar is also suggested in previous studies for *BeppoSAX*, XMM-Newton and *Swift*/XRT observations by Massaro et al. (2008) and Tramacere et al. (2007), while Giommi et al. (2002) favours the power-law model as a description of the *BeppoSAX* observations.

PKS 1510–089: The *Swift*/XRT spectrum of this blazar is best described with either a power-law or a log-parabola fit. The favourable N_H values are the ones provided by Kalberla et al. (2005) and free N_H value. For the log-parabola model also the N_H value taken from Dickey & Lockman (1990) gives satisfying result. The free N_H values are smaller than the values provided in the quoted surveys. χ_{red}^2 values of the preferred fits are close to 1.0.

Donato et al. (2005) found the broken power-law as the best description of *BeppoSAX* observations. Again, in this case, the break energy is found to be in the low energy part of the X-ray range i.e. $E_b = 1.41_{-0.25}^{+1.21}$ keV.

PG 1553+113: The X-ray spectrum can be well described using both a power-law and a log-parabola models, but in the first case only with the free N_H value. In the case of the log-parabola models similar values of $\chi_{red}^2 \sim 1.2$ are obtained using different N_H . The log-parabola model the different values of N_H result in very similar values of α and β parameters.

Massaro et al. (2008) and Tramacere et al. (2007) described the X-ray spectra with the curved log-parabola models. The object was also a target of studies by Donato et al. (2005), fitted the power-law and the broken power-law models, depending on the observation date. However Giommi et al. (2002) favour the log-parabola hypothesis, also for *BeppoSAX* monitoring. More recent multi-wavelength studies of the blazar confirmed preference of a convex curved model for *Swift*/XRT data (Aleksić et al. 2014b).

1ES 1959+650: A For the case of the log-parabola model χ_{red}^2 values are around 1.2-1.3, while in the case of the power-law model χ_{red}^2 is about 1.3 for the case of free N_H value and the one taken from survey by Willingale et al. (2013) and 2.0 in the other cases. In the case of the log-parabola fit with N_H value from Willingale et al. (2013) the β parameter is negative, which we do not find as a preferable description of the X-ray spectrum of this blazar, especially while the observations collected in the other wavelengths are considered.

Giommi et al. (2002); Donato et al. (2005); Tramacere et al. (2007) used the log-parabola model and the broken power-law one as preferred for X-ray spectrum of this blazar. In the recent multi-frequency studies of the source, including also *Swift*/XRT and RXTE-PCA data, the power-law model is found as a satisfactory description (Aliu et al. 2013, 2014a).

PKS 2005–489: The X-ray spectrum can be well characterized using the log-parabola and the power-law models. Also all values of N_H tested result in comparable values of $\chi_{red}^2 \sim 1.0$. All the spectral fits give very similar values of the fit parameters. The negative values of β suggest a concave

curvature, but the errors calculated for the parameter are large compared to the value. The curvature effect is caused by the high energy part of the spectrum, where only a few last spectral points rise.

In the previous works Donato et al. (2005) found the broken power-law as the best model to characterize *BeppoSAX* observations of PKS 2005–489, while Giommi et al. (2002); Tramacere et al. (2007); Massaro et al. (2008) suggested a description of *BeppoSAX*, XMM-Newton and *Swift*/XRT observations with the log-parabola model. Several multi-wavelength campaigns targeting the source also included the X-ray observations with different instruments, both in the low and the high states of the blazar. In most of these cases soft X-ray observations are well described with the single power-law model (e.g. Sambruna et al. 1995; Perlman et al. 1999; Tagliaferri et al. 2001; Rector et al. 2002; H.E.S.S. Collaboration 2010, 2011b).

PKS 2155–304: For the blazar the X-ray spectrum is well fitted using the log-parabola model. Different values of N_H tested result in comparable $\chi_{red}^2 \sim 1.1$, while in the case of the power-law model fitted $\chi_{red}^2 \sim 1.2$. Again, this is the case of blazar for which different values of N_H tested, for the power-law as well as the log-parabola model result in very similar values of the α , β , and Γ parameters.

In the earlier studies Donato et al. (2005) found the curved log-parabola model as the best description of *BeppoSAX* observations. The same model was successfully used by Giommi et al. (2002); Tramacere et al. (2007); Massaro et al. (2008) for *BeppoSAX*, XMM-Newton and *Swift*/XRT observations. The studies of XMM-Newton observations of PKS 2155–304 in 2006 revealed a curved shape of the spectrum and an indication of both synchrotron and inverse Compton components revealed in data (Zhang 2008). The results mentioned suggest that PKS 2155–304 can be a rare example of HBL type blazar for which possible up-turn point of SED is found in soft X-ray regime. However previous studies with *BeppoSAX* observations of the source were well described with the single power-law or the convex broken power-law model (e.g. Zhang et al. 1999; Chiappetti et al. 1999; Zhang et al. 2002).

Also during the multi-wavelength studies targeting the low state of the blazar X-ray spectrum was well characterized with the broken power-law model (Aharonian et al. 2009). Detailed, longterm spectral studies, including observations of the blazar obtained during the period of 2005-2012 with XMM-Newton has been successfully described with the log-parabola model (Kapanadze et al. 2014).

BL Lacertae: The X-ray spectrum of this blazars can be well fitted with the power-law as well as with the log-parabola model, but in both cases with free value of the Galactic absorption parameter and the one provided by Willingale et al. (2013). In the case of the X-ray spectrum of BL Lacertae different values of N_H tested, for the power-law as well as the log-parabola models, result in diametrically different values of the spectral and curvature parameters. Visual inspection of data suggests the curvature in the X-ray domain, but it is difficult to quantify, due to the high dispersion of data points in low energy part of the spectrum. For the preferable fits χ_{red}^2 is about 1.1-1.2.

Previous studies on this blazar's spectrum in the X-

ray energy band disentangle synchrotron and inverse Compton components in this range. Tanihata et al. (2000) found that for the blazar in the energy range below 1 keV a soft and steep spectrum is dominating, in contrast to hard component otherwise. Ravasio et al. (2002) reported two periods of observations of the blazar in 1999. In June the source has a concave spectrum with a very hard component above 5-6 keV, while in December data were well fitted with the power-law. Donato et al. (2005) found the spectrum well described with the broken power-law model with the break energy $E_b = 0.45_{-0.44}^{+0.39}$ keV. Also, the observations of BL Lacertae with INTEGRAL/IBIS are also well described with the broken power-law model with $E_b = 1.71_{-0.15}^{+0.75}$ keV. Raiteri et al. (2009) in the multi-wavelength studies including XMM-Newton observations of the source also unveiled a concave curvature in the X-ray regime. The curved model is also the preferable one for The *BeppoSAX* observations studied by Massaro et al. (2008), while Giommi et al. (2002) suggested the single power-law as the best description for *BeppoSAX* data.

B3 2247+381: The X-ray spectrum of this blazar is well characterized with the log-parabola model with any of N_H values tested. In each of the mentioned cases χ_{red}^2 is about 1.0. A good description of the spectrum is also given with the power-law model with free N_H value and the one provided by Willingale et al. (2013). For the other N_H values tested, the one provided by Kalberla et al. (2005) and by Dickey & Lockman (1990), χ_{red}^2 values are 1.6 and 1.3, respectively.

1ES 2344+514: The best description of the spectrum is given with the log-parabola model and a free Galactic absorption value as well as N_H provided by Kalberla et al. (2005) and Dickey & Lockman (1990). For these preferable cases χ_{red}^2 is about 1.1. The log-parabola fit with N_H from Willingale et al. (2013) survey results in the largest value of χ_{red}^2 of about 1.3 and negative value of the β parameter. As in the case of 1ES 0414+009, the β value is not consistent with the SED shape (see e.g. Aleksić et al. 2013). In the context of the power-law model a fit with a free value of the Galactic column density gives a satisfactory result.

Previous studies of the X-ray spectra obtained with *Swift*/XRT and *BeppoSAX* show that these data cover the synchrotron bump in its SED. The X-ray spectrum was usually well described with the power-law model (e.g. Giommi et al. 2000; Acciari et al. 2011; Aleksić et al. 2013). However a need for a curved model was found also for the case of *BeppoSAX* X-ray data by Massaro et al. (2008). It is also worth mentioning that 1ES 2344+514 exhibits strong spectral variability with the synchrotron peak shifting to higher energies during flares (Giommi et al. 2000). The synchrotron peak frequency during such events is at 10 keV or above, which classifies the source as the so-called extreme HBL.

5 BLAZARS WITH UPWARD-CURVED X-RAY SPECTRA

In the further studies we focus on five blazars for which a concave curvature of the spectrum suggests that both synchrotron and inverse Compton components are located in the X-ray regime. This gives a perfect opportunity to study

spectral and temporal variability of both components contemporaneously.

In the first step the longterm background-subtracted light curves for each source were inspected (upper panels of Fig. 8-12). In each case the presented light curves show observations from 2005 up to October 2014 collected with *Swift*/XRT in the PC mode in the energy range of 0.3-10 keV. Each light curve is binned in observation-length intervals.

In order to separate synchrotron and inverse Compton components we define the upturn energy (E_{upt}) being identical to the break energy value taken from the broken power-law fit, which is given in Table 5. We define two energy bands for each source. The soft band in the energy range (0.3 keV, E_{upt}) and the hard energy band (E_{upt} , 10 keV). Note that E_{upt} is kept constant for each source throughout the 10 years period. The variations in both bands and of the hardness ratio (HR), defined as the proportion of the count rate in the hard and the soft band, are shown in Fig. 8-12.

3C 66A: The light curve (see upper panel of Fig. 8) shows variability manifested mainly in one outburst in 2008. The flux changes are characterized by a fractional variability amplitude (Edelson & Krolik 1988) $F_{var} = (67 \pm 2)\%$ with the uncertainty calculated following Vaughan et al. (2003). Except for this outburst (with a count rate of ~ 0.7 count/s) the source flux level observed in different epochs is about 0.1-0.2 counts/s. The soft and the hard X-ray light curves in the energy bands of 0.3-3.4 keV and 3.4-10 keV, respectively are shown in Fig 8. The fractional variability amplitudes for the soft and hard bands are following: $F_{var} = (69 \pm 2)\%$ and $F_{var} = (56 \pm 1)\%$, respectively. The hardness ratio is characterized by a fractional variability amplitude of $F_{var} = (28 \pm 1)\%$. Hence, the most pronounced variability is observed in the soft energy band.

To investigate the spectral variability of 3C 66A in detail, spectra have been obtained during three intervals, shown in Fig. 8. The division takes into account the exposure for spectral analysis in each interval and the range of different flux levels for the source. The assumes a monotonous change of spectral properties with the total flux even if several distinct flares are coadded. In the first interval there are only two observations performed in 2005, but the second one has an exposure of 52 ks. For each of the selected intervals, data are fitted with the broken power-law model with the Galactic absorption (N_H value taken from LAB survey), which describe the overall spectrum well. The spectral parameters are collected in Table 6. The plots presenting SEDs for all intervals are shown in Fig. 13. In Sect. 4 it was shown that the average spectrum is characterised by concave curvature and an upturn energy of about 3.4 keV. This value is an average one and the soft and hard intervals selected in Fig. 8 do not reflect precisely the synchrotron and the inverse Compton components for all times. The concave shape of the spectrum is clearly visible in the first interval. For the other intervals the upturn is not visible and the spectrum in the energy band presents only a synchrotron component. Since the third epoch display the source at a fainter state compared to the first one, the absence of an upturn implies flux variability of the inverse Compton component.

Figure 14 presents the comparison of the hardness ratio and the total count rate. There is no clear trend between

these quantities. The soft spectral state is observed in bright or faint, while the hard state of the source is for faint state.

S5 0716+714: The source, known for its variability, clearly manifests this feature in the longterm light curve presented in the upper panel of Fig. 11. The middle panels of Fig. 11 shows the hard and soft light curves, for which the energy bands are defined as 1.1-10 keV and 0.3-1.1 keV, respectively. The longterm variability is characterized by fractional variability amplitude for the total, soft and hard bands resulting in $F_{var} = (61 \pm 1)\%$, $F_{var} = (75 \pm 1)\%$ and $F_{var} = (52 \pm 1)\%$, respectively. For the comparison the hardness ratio light curve (see bottom panel in Fig. 11) results in $F_{var} = (22 \pm 2)\%$. Then, the most prominent variability is observed in the soft energy range.

To study the spectral variability we divide the light curve into four intervals (see Fig. 11). The first interval includes only two observations, but the first one has the time exposure of 19 ks. Each of the spectrum, for selected intervals, can be well characterized with the broken power-law model with the Galactic absorption N_H value from DL survey. The spectral parameters are collected in Table 6 and the corresponding plots are shown in Fig. 13. All the selected intervals have similar value of the break energy, between 0.9 and 1.4 keV. The overall the broken power-law fit to data results in the break energy of 1.1 keV. This indicates that division into the soft and the hard intervals with a good approximation reflects synchrotron and inverse Compton components. We also investigate the spectral variability in the context of flux variation. Hardness ratio - total count rate comparison, presented in Fig. 14 indicates behaviour similar to the one observed in the case of 3C 66A. It is also worth mentioning that in the case of this source we do not see clear harder-when-brighter trend or the opposite softer-when-brighter one. While the anticorrelation of the hardness ratio and the flux count rate in the case of S5 0716+714 was previously reported in the X-ray regime by e.g. Foschini et al. (2006); Ferrero et al. (2006). The values of the spectral indices indicate significant spectral variability of the synchrotron component, which is not observed in the case of the inverse Compton part of the spectrum.

W Comae: The observed count flux rate (see the upper panel of Fig. 9) changes in the range of 0.1-0.7 counts/s. The figure shows also the soft (0.3-2.0 keV) and the hard (2.0-10.0 keV) energy band light curve as well as the hardness ratio evolution. The longterm variability of the blazar can be characterized with fractional variability amplitude resulting in $F_{var} = (94 \pm 1)\%$, $F_{var} = (69 \pm 2)\%$, $F_{var} = (56 \pm 6)\%$, and $F_{var} = (28 \pm 9)\%$ for the total, the soft, the hard and hardness ratio light curve respectively. These results show that the highest variability is observed in the energy range of 0.3-10 keV.

As in the case of previously discussed sources, separate intervals are distinguished to investigate spectral features in the different states. In the case of W Comae two intervals are considered representing the low (the second interval) and the elevated (the first interval) flux level (see Fig. 9). Data collected during both periods are fitted with the broken power-law model with the Galactic absorption N_H taken from the survey provided by Willingale et al. (2013). The spectral fit parameters are collected in Table 6, while all correspond-

ing plots are shown in Fig.13. In both intervals the spectral shapes reveal a concave curvature. The selected intervals are characterized with different values of the break energy: 4.1 keV and 1.2 keV for the first and the second interval, respectively. It is worth reminding here that the crossing point in the broken power-law fit to all data is determined as 2.0 keV. Because of this fact the soft and the hard energy bands used for the light curves do not indicate clearly the synchrotron and inverse Compton components. The values of the spectral indices reveal larger spectral variability in the soft energy band. The comparison of the hardness ratio and the total count rate, presented in Fig. 14 exhibit similar behaviour as in the case of 3C 66A and S5 0716+714.

4C +21.35: The light curve presenting the longterm variability of the blazar (see the upper panel of Fig. 12) shows smaller changes in the observed count rate than in the case of other blazars discussed here. The variability observed in the energy range of 0.3-10 keV can be described with fractional variability amplitude as high as $F_{var} = (39 \pm 1)\%$. The soft and the hard energy bands, presented in the middle panels of Fig. 12, are defined as: 0.3-1.2 keV and 1.2-10 keV. The value of 1.2 keV is the break energy point found in the average spectrum of this blazar. To check whether the fractional variability amplitude depends on the energy band considered, this quantity has been also calculated for the soft and the hard energy bands resulting in: $F_{var} = (56 \pm 1)\%$ and $F_{var} = (31 \pm 1)\%$, respectively. The bottom panel in Fig. 12 show hardness ratio light curve, which is characterized by $F_{var} = (23 \pm 1)\%$.

Three intervals have been distinguished for detailed spectral studies. The spectral analysis has been repeated for each of the interval. Since in the case of set of all observations data are well described with broken power-law model with the Galactic absorption, here also this model has been used. For this case N_H value taken from Willingale et al. (2013) survey is used. Reduced χ^2 values show that this model works well also for shorter intervals. All the spectral parameters of the broken power-law fit and the corresponding plots are collected in Table 6 and shown in Fig. 13. For the intervals selected the broken power-law fit results in the break energy of value 1.0-1.2 keV. We can then conclude that the soft and the hard energy bands with a good approximation correspond to the synchrotron and the inverse Compton spectral components, respectively. The comparison of the hardness ratio and the total count rate, presented in Fig. 14 shows complex behaviour, with individual substructures and indication for hysteresis effects visible within each.

BL Lacertae: The light curve of BL Lacertae (see upper panel of Fig. 10) in the energy range of 0.3-10 keV shows significant variability exhibited in several outbursts. The longterm variability is characterized using fractional variability amplitude with the value of $F_{var} = (52 \pm 1)\%$. As in the previous cases, we also consider the soft and the hard energy bands defined as 0.3-1.1 keV and 1.1-10.0 keV, respectively, as well as the hardness ratio. The variability in the soft and the hard energy ranges is then given by $F_{var} = (47 \pm 1)\%$ and $F_{var} = (58 \pm 1)\%$, respectively. The variability amplitude is more pronounced in the higher en-

ergies. For the comparison the hardness ratio variability is quantified by $F_{var} = (13 \pm 1)\%$.

To check if the crossing point, disentangling the synchrotron and the inverse Compton components, is shifting for the different flux states of the source, four intervals are distinguished (see the light curve in Fig. 10). Each of the intervals represents different the X-ray behaviour of BL Lacertae. Data in each interval are then fitted with the broken power-law model with the Galactic absorption N_H taken from the survey provided by Willingale et al. (2013). The fit parameters are collected in Table 6 and the corresponding plots are shown in Fig. 13. Let us here remind that the broken power-law fit to all data results in the break energy of 1.1 keV. For the shorter intervals the break energy is oscillating between 1.1-1.2 keV. A clear upturn of the spectrum, disentangling two spectral components is visible in the case of the three intervals discussed.

Furthermore, there is no significant shift of the crossing point to the higher energies with the increasing flux, which is observed in the other blazars discussed. Hence, for this blazar the soft and hard energy bands in a good approximation correspond to the synchrotron and the inverse Compton components. The synchrotron component is then characterized by larger spectral variability comparing to the inverse Compton one. The hardness ratio seem to be correlated with the total count rate (see Fig. 14), which is not surprising in the case of HBL type blazars, but it is not a common feature of the IBL ones.

6 SUMMARY AND CONCLUSIONS

In this paper we study spectra of 29 TeV γ -ray emitting blazars including 22 HBL, 4 IBL type blazars, and 3 FSRQs observed with *Swift*/XRT in the energy range of 0.3-10 keV. The only one LBL blazar detected in TeV γ -ray regime, (AP Librae) is not part of the sample presented here. Since only TeV blazars are included in the sample and HBL type objects are known to be the brightest in this regime, three groups of blazars included are not distributed uniformly.

The spectra studied are averaged, which means that they include observations in the low and the high states, for data collected since the mission start up to October 2014. We focus only on the PC mode observations, which implicates that the highest outbursts are not included in the averaged spectra. This is the first spectral survey including 10 years of observations of TeV emitting blazars collected with *Swift*/XRT.

We conclude that the most of the spectra are well described using the curved log-parabola model. Only in a few cases we get better characteristics with the power-law model. These are 1ES 1101–232, Mrk 180, and PKS 2005–489. There are also a few cases of objects for which we got acceptable power-law fit only if the free N_H value is used. These are mainly cases for which free value of the Galactic absorption is much higher than the ones provided in the discussed surveys.

The curved log-parabola model has been used to describe the shape of radio-optical blazars spectra for the first time by Landau et al. (1986). The first X-ray studies involving the log-parabola as the best model for spectral fits have been performed by Giommi et al. (2002) who found

this model as the preferable one for 50% of blazars studied. Also Massaro et al. (2004b,a); Tramacere et al. (2007); Massaro et al. (2008) successfully used this model in their X-ray spectral studies.

The observed convex curvature in the X-ray spectra is likely to result from a single accelerated particle distribution (e.g. Massaro et al. 2004a). The concave curvature observed may be caused by the fact that the X-ray range is a place, where synchrotron and inverse Compton components meet and the curvature is a consequence of the spectral upturn. In the latter case the X-ray observations enable simultaneous study of the low and the high energy ends of the particle distribution function.

Different values of N_H tested do not allow us to find one universal set. On the other hand we cannot conclude that any of mentioned N_H surveys can be used in each case to obtain good fit. But we can then summarize that each case should be treated separately, often including wider view on spectral features also in different wavelengths, see an example of two blazars presented in Fig. 15, where the *Swift*/XRT observations are combined with the *Swift*/BAT ones. Furthermore, our studies has shown that the Galactic column density value influence the overall spectral fit. In general larger N_H values result in softer spectral index, i.e. larger value of Γ or α parameter in the power-law and the log-parabola model, respectively. Also in most cases for the log-parabola model fitted the curvature parameter is larger for smaller N_H values. Hence, we can summarize that the choice has significant influence on the X-ray spectral features. It is also worth mentioning that χ^2_{red} is not a good indicator, which could be used to distinguish the most accurate value of the Galactic column density. Let us here remind the example of 1ES 0033+595, for which very different values of N_H result in the significantly different spectral fit parameters and very similar values of χ^2_{red} (see Fig. 6 and 2 (in the online material), and Table 3 and 4 (in the online material) for plots and spectral fit parameters for the log-parabola and the power-law models). In the mentioned case too small value of N_H e.g. the one taken from LAB survey result in the spectral shape with the artificial bump which cannot be easily explained. Very similar situation take place for the cases of blazars such like 1ES 0502+675, 1ES 0647+250 or 1ES 1959+650.

The log-parabola model is described by the α parameter, which corresponds to the spectral index and β one, which characterize the spectral curvature. We found the spectral indices α in the range of 1.4-2.6.

The performed spectral studies of 29 γ -ray emitting blazars allow us to distinguish only 5 blazars for which the concave spectral shape indicates that in the X-ray regime synchrotron and inverse Compton components meet. Since the spectral upturn is expected in all blazar SEDs and we focused on the energy range of one magnitude, we then conclude that the spectral upturns are distributed in the broad range of energies. The second part of the paper includes detailed temporal and spectral studies focused on 5 sources for which concave shape of the spectrum indicates that the synchrotron and the inverse Compton components meet in the X-ray regime. The mentioned sources are: 4C+21.35, S5 0716+714, BL Lacertae, 3C 66A, and W Comae. For each of the objects the preferable model to describe the spectral shape is the log-parabola with a concave curvature. For these

five blazars with the upturn, we fit spectra with the broken power-law model, which helps us to find the crossing point for the average spectrum, disentangling the synchrotron and the inverse Compton components. For all sources the upturn point is clearly visible in the averaged spectrum for the dataset including all data analysed. But for the case of shorter time intervals synchrotron and inverse Compton components are not always visible. For example 3C 66A for A and B intervals two components are clearly visible, while for the case of the third distinguished interval, the spectral shape reveals only the synchrotron part of the spectrum. It is also worth underlining that the upward curvature was previously reported for S5 0716+714 (Cappi et al. 1994; Giommi et al. 1999; Tagliaferri et al. 2003; Donato et al. 2005; Ferrero et al. 2006), BL Lacertae (Tanihata et al. 2000; Ravasio et al. 2002; Donato et al. 2005), 3C 66A (Donato et al. 2005), and W Comae (Tagliaferri et al. 2000; Donato et al. 2005), while this is the first case when the upturn between the synchrotron and the inverse Compton component is found for 4C +21.35. Using *Swift*/XRT observations of blazars we found five objects with the spectral upturn. Also, there are objects for which single *Swift*/XRT observations do not reveal this feature, but joint spectrum, that include *Swift*/XRT and *Swift*/BAT data show such an upturn. But since *Swift*/BAT spectra are longterm-averaged it is difficult to quantify the number of such objects. As an example Fig. 15 show joint fits for PKS 0548-322 and PKS 2005-489.

The longterm variability of those five blazars has been characterized with fractional variability amplitude. This quantity is also calculated for the distinguished the soft and the hard energy bands as well as for the hardness ratio evolution. The soft and the hard energy band corresponds to the synchrotron and the inverse Compton components in the average spectral fit. For 4C +21.35, S5 0716+714, 3C 66A, and W Comae the largest value of F_{var} is obtained for the soft energy range, while the lowest variability is observed for the hardness ratio light curve. Only for BL Lacertae the largest value of F_{var} is for the hard energy range.

We also investigate the spectral variability by dividing the light curves into shorter intervals and performing spectral analysis for smaller data sets. In this case only the broken power-law model with the Galactic absorption value taken from LAB survey is tested. In the case of S5 0716+714, 4C +21.35 and BL Lacertae the energy break value are consistent within errors with the value obtained for the average spectrum. Hence, we conclude that the distinguished soft and the hard energy bands corresponds to the synchrotron and the inverse Compton components, respectively. In the case of 3C 66A, and W Comae the break energy values for the short intervals and the average spectrum are different, so the soft and the hard bands can not be unambiguously associated with the synchrotron and the inverse Compton components. Furthermore the comparison of the spectral indices for the broken power-law fit for the shorter intervals revealed significant variability in the soft energy range, while in the hard one the variability is not noticed in the case of 3C 66A.

We also compared the hardness ratio, calculated as a ratio of count rates in the hard and the soft energy bands, with the total intensity. This comparison revealed different behaviours of in HR-total intensity diagrams. For three of studied blazars, namely 3C 66A, W Comae and S5 0716+714

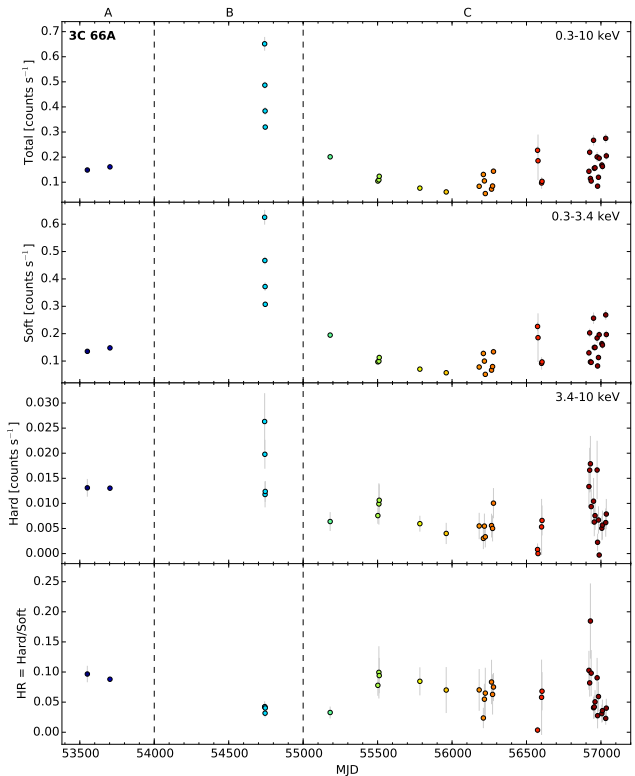


Figure 8. The longterm count rate and the hardness ratio light curve for 3C 66A. The following panels present: counts rate in energy range of 0.3-10 keV; the soft energy band of count flux (0.3-3.4 keV); the hard energy band of count rate (3.4-10 keV); the hardness ratio defined as ratio of hard and soft energy band count rate. The vertical dashed lines indicate selected intervals discussed in Sect. 5. Different colours of data points indicate the time of a given measurement. The earliest pointings are denoted by dark blue symbols and the most recent ones depicted in red. The same colour coding is used in Fig. 14.

for the soft spectrum (smaller values of HR) total intensity of the sources changes in the whole range of brightness. While when the source is faint, different values of HR can be observed. Such a behaviour suggests that in the faint state of the source the influence of the inverse Compton component is more significant. For BL Lacertae HR-total intensity diagram exhibit harder-when-brighter trend. Such a behaviour is a common feature for HBL type blazars (e.g. Pian et al. 1998; Zhang et al. 2005, 2006; H.E.S.S. Collaboration 2012), while IBL and LBL ones often exhibits softer-when-brighter pattern (e.g. Giommi et al. 1999; Ravasio et al. 2002; Ferrero et al. 2006). The case of 4C 21.35 is the most complex one with individual substructures and an indication for hysteresis effects visible within each. Such a hysteresis trend visible in HR-flux diagram can be related to the changes of the acceleration and cooling time scales (Kirk et al. 1998).

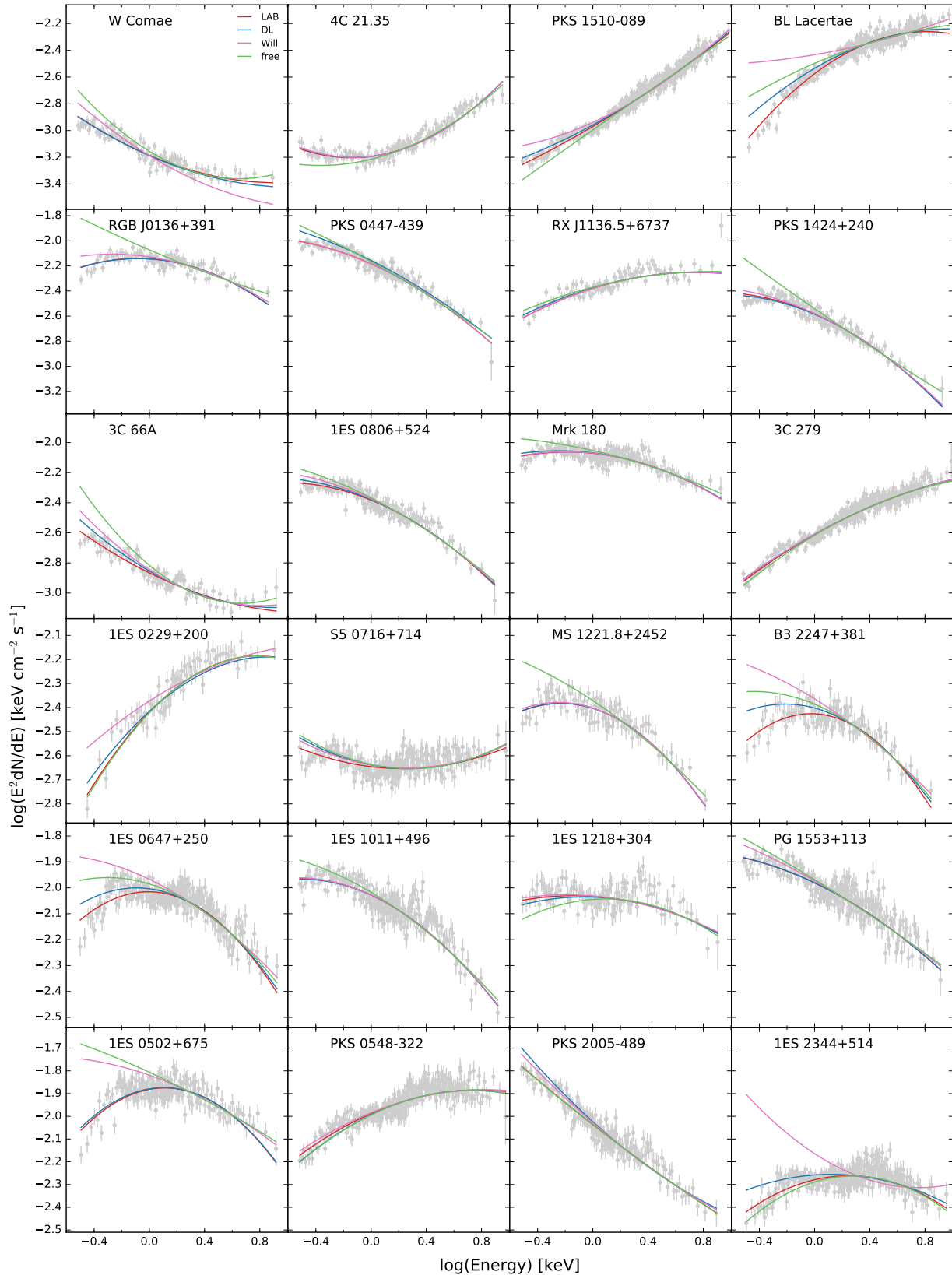


Figure 1. The X-ray spectral energy distributions of 29 selected blazars sorted by increasing flux density. The names of the sources are given in the upper part of each panel. Four log-parabola spectral models with different values of N_H are presented in different colours: red – N_H taken from the LAB survey (Kalberla et al. 2005), blue – N_H value taken from Dickey & Lockman (1990), magenta – N_H value taken from Willingale et al. (2013) and green – free N_H value. Data (grey points) presented in the figure are those fitted with the log-parabola model with the Galactic absorption value taken from LAB survey.

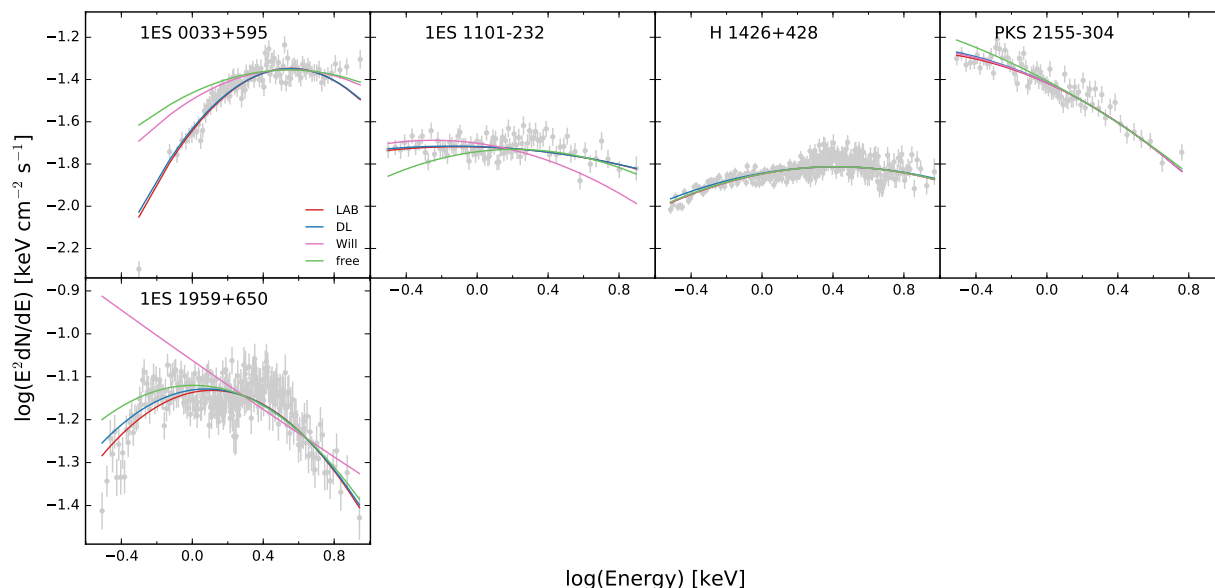


Figure 1 – continued

Figure 2. The X-ray spectral energy distributions of 29 selected blazars sorted by increasing flux density. The names of the sources are given in the upper part of each panel. Four power-law models using different values of N_H are presented using different colours: red – N_H taken from the LAB survey (Kalberla et al. 2005), blue – N_H value taken from Dickey & Lockman (1990), magenta – N_H value taken from Willingale et al. (2013) and green – free N_H value. Data (grey points) presented in the figure are those fitted with the power-law model with the Galactic absorption value taken from LAB survey. The figure is available in the online material only.

Figure 3. The X-ray spectra fitted with the log-parabola model with the Galactic absorption value taken from LAB survey and the ratios (data points divided by the folded model). The plots present spectra for: 1ES 0033+595, RGB J0136+391, 3C 66A, 1ES 0229+200, PKS 0447-437, 1ES 0502+675. The name of each object is also given in the upper right corner of each plot.

Figure 4. The X-ray spectra fitted with the log-parabola model with the Galactic absorption value taken from LAB survey and the ratios (data points divided by the folded model). The following plots present spectra for: PKS 0548-322, 1ES 0647+250, S5 0716+714, 1ES 0806+524, 1ES 1011+496, 1ES 1101-232. The name of each object is also given in the upper right corner of each plot.

Figure 5. The X-ray spectra fitted with the log-parabola model with the Galactic absorption value taken from LAB survey and the ratios (data points divided by the folded model). The following plots present spectra for: Mrk 180, RX J1136.5+6737, 1ES 1218+304, W Comae, MS 1221.8+2452, 4C 21.35. The name of each object is also given in the upper right corner of each plot.

Figure 6. The X-ray spectra fitted with the log-parabola model with the Galactic absorption value taken from LAB survey and the ratios (data points divided by the folded model). The following plots present spectra for: 3C 279, PKS 1424+240, H 1426+428, PKS 1510-089, PG 1553+113, 1ES 1959+650. The name of each object is also given in the upper right corner of each plot.

Figure 7. The X-ray spectra fitted with the log-parabola model with the Galactic absorption value taken from LAB survey and the ratios (data points divided by the folded model). The following plots present spectra for: PKS 2005-489, PKS 2155-304, BL Lacertae, B3 2247+381, 1ES 2344+514. The name of each object is also given in the upper right corner of each plot.

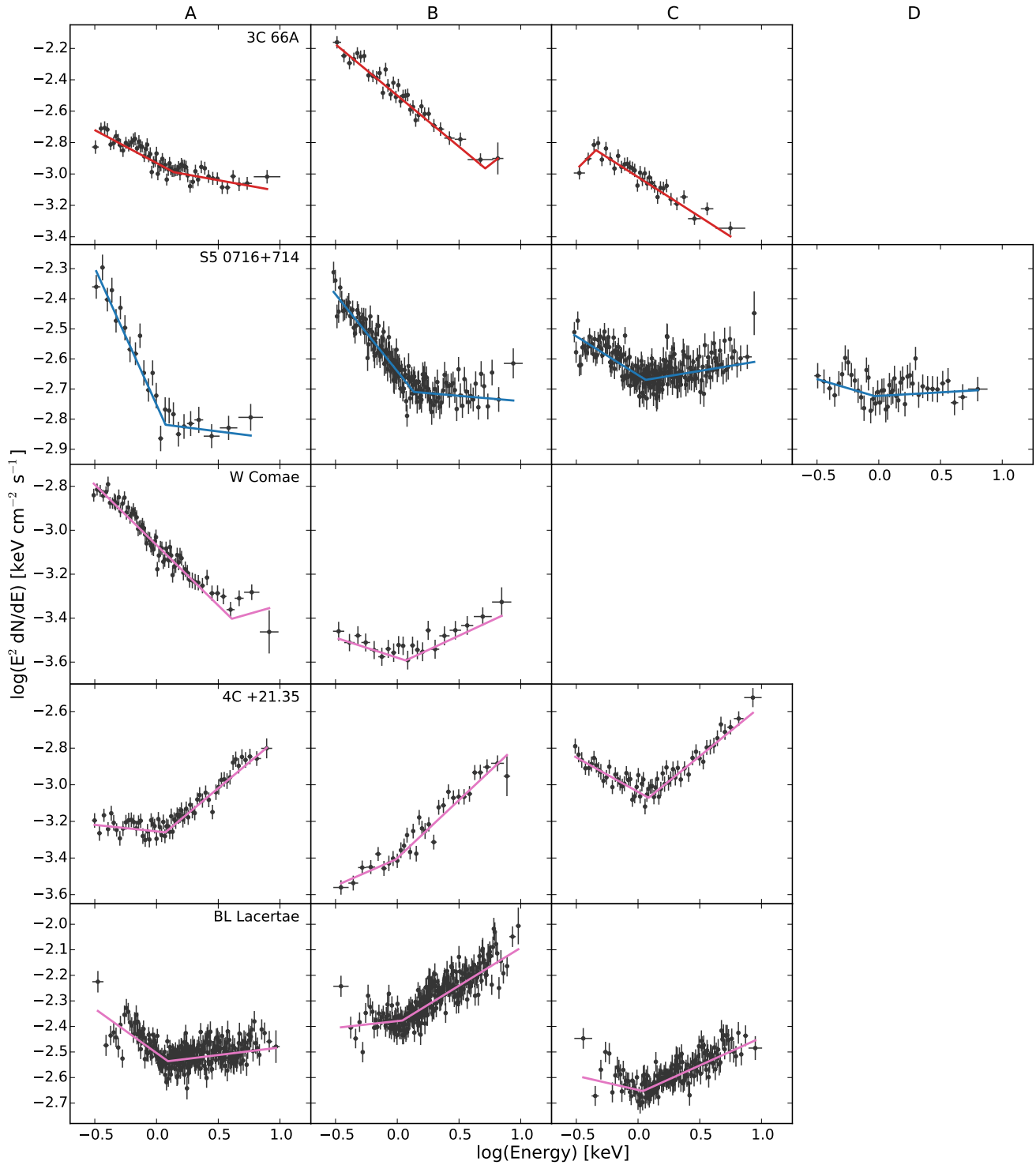


Figure 13. Spectral energy distributions for spectral fits with broken power-law models during periods defined in Fig. 8-12 for 3C 66A, S5 0716+714, W Comae, 4C 21.35 and BL Lacertae. While both spectral components change in slope and flux normalization, the upturn energy (E_{upt}) does not display variations.

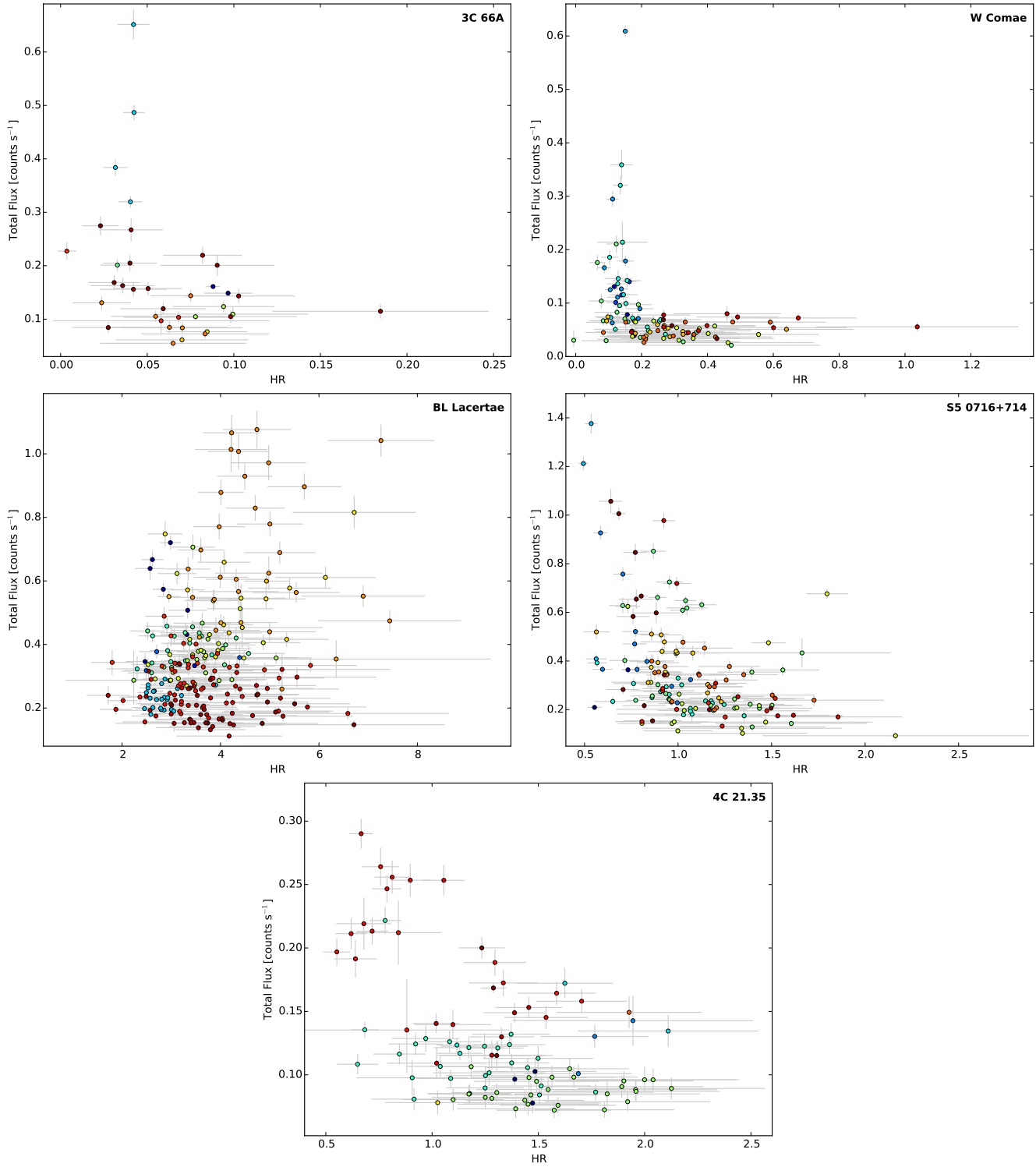


Figure 14. The comparison of the flux (total count rate) and the hardness ratio for 3C 66A, W Comae, BL Lacertae, S50716+714 and 4C 21.35. The soft and hard bands are chosen as described in Sect. 5 and presented in Fig. 8-12. The colour of a given data point indicates the time of a given measurement. The earliest observations are denoted by dark blue symbols and the most recent ones depicted in red, with the rainbow colour scale normalized to the entire span of the *Swift*/XRT observations of a given blazar. The same colour coding is used in Fig.8-12.

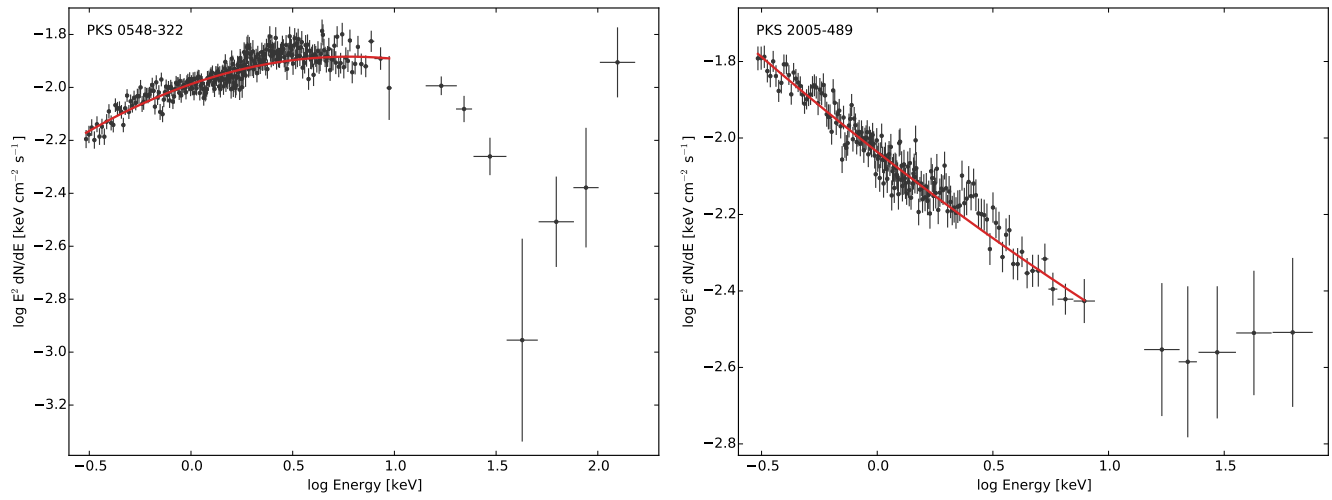


Figure 15. The examples of joint spectral energy distributions including *Swift*/XRT and *Swift*/BAT data for PKS 0548-322 and PKS 2005-489. Each plot presents *Swift*/XRT data fitted with a log-parabola model, and the N_H value taken from LAB survey, and BAT data from the 70-Month Hard X-ray Survey (Baumgartner et al. 2013).

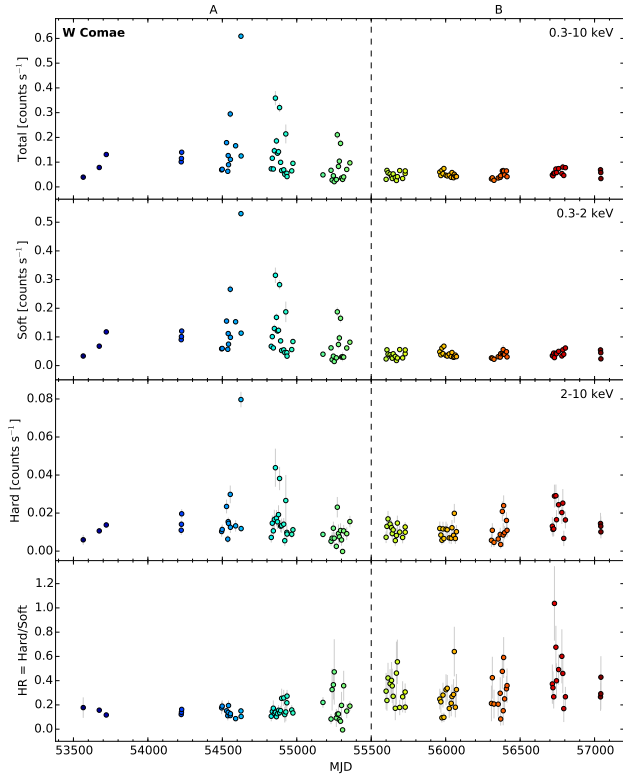


Figure 9. The longterm count rate and the hardness ratio light curve for W Comae. The following panels present: counts rate in energy range of 0.3-10 keV; the soft energy band of count flux (0.3-2.0 keV); the hard energy band of count rate (2.0-10 keV); the hardness ratio defined as ratio of hard and soft energy band count rate. The vertical dashed line indicates selected intervals discussed in Sect. 5. Different colours of data points indicate the time of a given measurement. The earliest pointings are denoted by dark blue symbols and the most recent ones depicted in red. The same colour coding is used in Fig. 14.

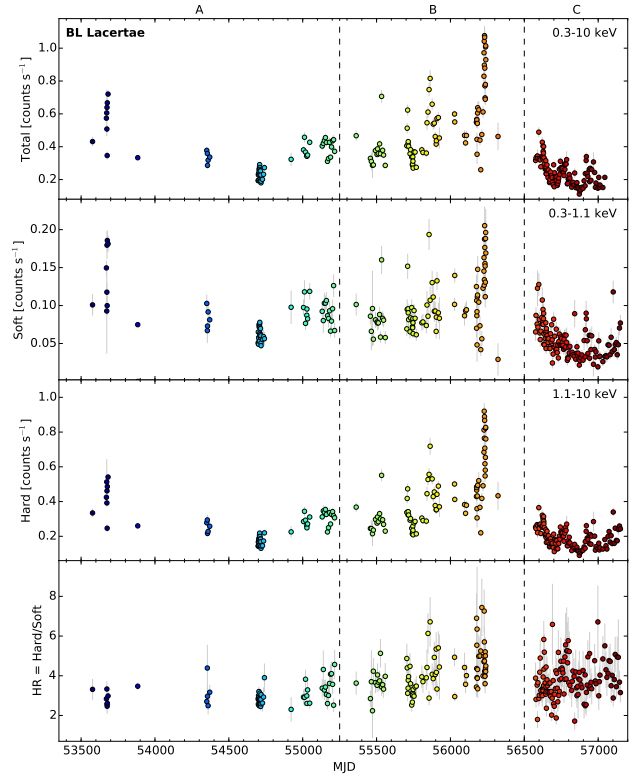


Figure 10. The longterm count rate and hardness ratio light curve for BL Lacertae. The following panels present: counts rate in energy range of 0.3-10 keV; the soft energy band of count flux (0.3-1.1 keV); the hard energy band of count rate (1.1-10 keV); the hardness ratio defined as ratio of hard and soft energy band count rate. The vertical dashed lines indicate selected intervals discussed in Sect. 5. Different colours of data points indicate the time of a given measurement. The earliest pointings are denoted by dark blue symbols and the most recent ones depicted in red. The same colour coding is used in Fig. 14.

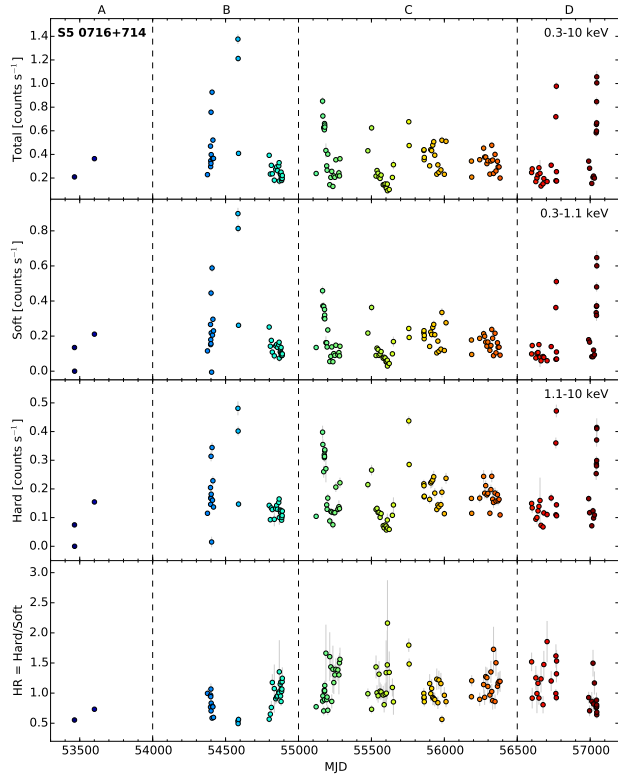


Figure 11. The longterm count rate and hardness ratio light curve for S5 0716+714. The following panels present: counts rate in energy range of 0.3-10 keV; the soft energy band of count flux (0.3-1.1 keV); the hard energy band of count rate (1.1-10 keV); the hardness ratio defined as ratio of hard and soft energy band count rate. The vertical dashed lines indicate selected intervals discussed in Sect. 5. Different colours of data points indicate the time of a given measurement. The earliest pointings are denoted by dark blue symbols and the most recent ones depicted in red. The same colour coding is used in Fig. 14.

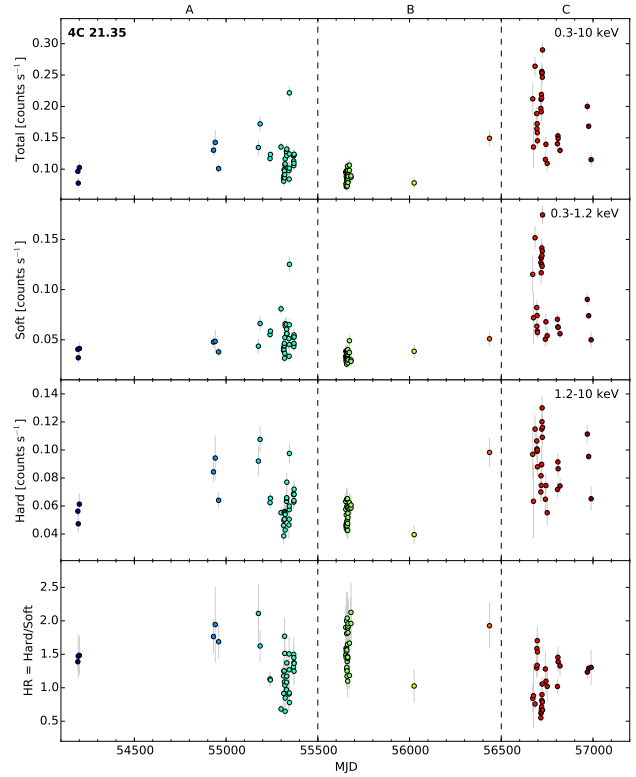


Figure 12. The longterm count rate and hardness ratio light curve for 4C 21.35. The following panels present: counts rate in energy range of 0.3-10 keV; the soft energy band of count flux (0.3-1.2 keV); the hard energy band of count rate (1.2-10 keV); the hardness ratio defined as ratio of hard and soft energy band count rate. The vertical dashed lines indicate selected intervals discussed in Sect. 5. Different colours of data points indicate the time of a given measurement. The earliest pointings are denoted by dark blue symbols and the most recent ones depicted in red. The same colour coding is used in Fig. 14.

Table 1. The summary of TeV blazars. (1) The object name, (2) the right ascension, (3) the declination, (4) the type of the blazar, (5) the redshift, (6) the integrated flux for *Swift*/XRT observations in PC mode in the energy range of 0.3-10 keV, (7) the exposure for *Swift*/XRT observations in PC mode in the energy range of 0.3-10 keV, (8) the product of (6) and (7), (9) the information if the blazar has been selected for the further detailed studies; selected objects are marked with + sign.

Object	RA <i>h m s</i>	DEC <i>° ' "</i>	type	redshift	PC flux $10^{-12} \text{ erg cm}^{-2} \text{ s}^{-1}$	PC exposure ks	PC flux · exposure $10^{-11} \text{ erg cm}^{-2}$	notes
(1)	(2)	(3)	(4)	(5)	(6)	(7)	(8)	(9)
SHBL J001355.9–185406 ¹	00 13 52.0	–18 53 29	HBL	0.095 ^a	12.30	14.4	1.77	
KUV 00311–1938 ²	00 33 34.2	–19 21 33	HBL	0.61 ^b	8.10	19.3	1.56	
1ES 0033+595 ³	00 35 52.6	+59 50 05	HBL	>0.24 ^c	109.90	15.2	16.70	+
RGB J0136+391 ⁴	01 36 32.5	+39 06 00	HBL	Unknown	23.80	18.8	4.47	+
RGB J0152+017 ⁵	01 52 33.5	+01 46 40	HBL	0.08 ^d	6.58	27.1	1.78	
3C 66A ⁶	02 22 41.6	+43 02 35	IBL	0.41 ^e	5.14	92.4	4.75	+
1ES 0229+200 ⁷	02 32 53.2	+20 16 21	HBL	0.14 ^f	20.70	22.4	4.64	+
PKS 0301–243 ⁸	03 03 23.5	–24 07 36	HBL	0.2657 ^c	8.38	25.2	2.11	
IC 310 ⁹	03 16 43.0	+41 19 29	HBL	0.0189 ^g	6.60	68.0	4.49	
RBS 0413 ¹⁰	03 19 47.0	+18 45 42	HBL	0.19 ^h	10.70	7.3	0.78	
1ES 0347–121 ¹¹	03 49 23.0	–11 58 38	HBL	0.188 ^c	43.70	3.2	1.40	
1ES 0414+009 ¹²	04 16 53.0	+01 05 20	HBL	0.287 ⁱ	18.30	6.2	1.13	
PKS 0447–439 ¹³	04 49 28.2	–43 50 12	HBL	0.107 ^j	24.60	50.5	12.42	+
1ES 0502+675 ¹⁴	05 07 56.2	+67 37 24	HBL	0.341 ^k	49.60	39.9	19.79	+
VER J0521+211 ¹⁵	05 21 45.0	+21 12 51	IBL	0.108 ^l	Not enough data in the PC mode to constrain spectral parameters.			
PKS 0548–322 ¹⁶	05 50 38.4	–32 16 12	HBL	0.069 ^m	55.70	103.1	57.43	+
RX J0648.7+1516 ¹⁷	06 48 45.6	+15 16 12	HBL	0.179 ⁿ	12.40	10.6	1.31	
1ES 0647+250 ¹⁸	06 50 46.5	+25 03 00	HBL	0.45 ^o	31.80	71.4	22.71	+
RGB J0710+591 ¹⁹	07 10 26.4	+59 09 00	HBL	0.125 ⁿ	Not enough data in the PC mode to constrain spectral parameters.			
S5 0716+714 ²⁰	07 21 53.4	+71 20 36	IBL	0.31 ^h	11.18	231.0	25.83	+
1ES 0806+524 ²¹	08 09 59.0	+52 19 00	HBL	0.137 ^p	14.68	51.9	7.62	+
RBS 0723 ²²	08 47 12.9	+11 33 50	HBL	0.198 ^p	19.60	7.1	1.39	
1RXS J101015.9–311909 ²³	10 10 15.0	–31 18 18	HBL	0.143 ^q	13.0	3.7	0.48	
S4 0954+65 ²⁴	09 58 47.0	+65 33 55	FSRQ	0.368 ^r	3.48	68.8	2.39	
1ES 1011+496 ²⁵	10 15 04.1	+49 26 01	HBL	0.212 ^s	34.30	58.5	20.07	+
1ES 1101–232 ²⁶	11 03 36.5	–23 29 45	HBL	0.186 ^h	90.10	12.5	11.26	+
Markarian 421 ²⁷	11 04 19.0	+38 11 41	HBL	0.031 ^t	Not enough data in the PC mode to constrain spectral parameters.			
Markarian 180 ²⁸	11 36 26.4	+70 09 27	HBL	0.046 ^r	37.90	50.7	19.22	+
RX J1136.5+6737 ²⁹	11 36 30.1	+67 37 04	HBL	0.1342 ^p	20.70	21.0	4.35	+
1ES 1215+303 ³⁰	12 17 48.5	+30 06 06	HBL	0.237 ^u	6.11	47.5	2.90	
1ES 1218+304 ³¹	12 21 26.3	+30 11 29	HBL	0.183 ^p	33.30	21.6	7.19	+
W Comae ³²	12 21 31.7	+28 13 59	IBL	0.103 ^p	3.13	166.3	5.21	+
MS 1221.8+2452 ³³	12 24 24.2	+24 36 24	HBL	0.218 ^v	15.60	28.2	4.40	+
4C +21.35 ³⁴	12 24 54.4	+21 22 46	FSRQ	0.435 ^m	4.95	174.3	8.63	+
S3 1227+25 ³⁵	12 30 14.1	+25 18 07	IBL	0.135 ^w	Not enough data in the PC mode to constrain spectral parameters.			
3C 279 ³⁶	12 56 11.1	–05 47 22	FSRQ	0.538 ^x	15.03	595.6	89.52	+
1ES 1312–423 ³⁷	13 14 58.5	–42 35 49	HBL	0.105 ^h	28.20	4.8	1.35	
PKS 1424+240 ³⁸	14 27 00.0	+23 47 40	HBL	0.390 ^y	9.03	49.8	4.50	+
H 1426+428 ³⁹	14 28 32.6	+42 40 21	HBL	0.129 ^p	59.20	123.6	73.17	+
1ES 1440+122 ⁴⁰	14 42 48.3	+12 00 40	HBL	0.1631 ^p	19.20	7.6	1.46	
PKS 1441+25 ⁴¹	14 43 56.9	+25 01 44	FSRQ	0.939 ^z	0.55	3.7	0.02	

Table 1 – *continued*

	(1)	(2)	(3)	(4)	(5)	(6)	(7)	(8)	(9)
PKS 1510–089 ⁴²	15 12 52.2	–09 06 21	FSRQ	0.360 ^m	10.51	362.0		38.05	+
AP Librae ⁴³	15 17 41.8	–24 22 19	LBL	0.049 ^c	6.36	32.7		2.08	
PG 1553+113 ⁴⁴	15 55 44.7	+11 11 41	HBL	>0.62 ^{aa}	43.70	86.5		37.80	+
Markarian 501 ⁴⁵	16 53 52.2	+39 45 37	HBL	0.037 ^x	Not enough data in the PC mode to constrain spectral parameters.				
Markarian 501 ⁴⁵	16 53 52.2	+39 45 37	HBL	0.037 ^x	0.0	0.0		0.0	
H 1722+119 ⁴⁶	17 25 04.3	+11 52 15	HBL	0.018 ^h	10.65	2.7		0.29	
1ES 1727+502 ⁴⁷	17 28 18.6	+50 13 10	HBL	0.055 ^{ab}	16.30	5.5		0.90	
1ES 1741+196 ⁴⁸	17 43 57.8	+19 35 09	HBL	0.083 ^{ac}	11.70	18.8		2.20	
HESS J1943+213 ⁴⁹	19 43 55.0	+21 18 08	HBL	>0.14 ^{ad}	20.60	13.7		2.82	
1ES 1959+650 ⁵⁰	19 59 59.8	+65 08 55	HBL	0.047 ^x	270.00	30.2		81.54	+
MAGIC J2001+435 ⁵¹	20 01 13.5	+43 53 02	IBL	< 0.2 ^{ae}	2.11	62.2		1.31	
PKS 2005–489 ⁵²	20 09 27.0	–48 49 52	HBL	0.071 ^m	31.00	50.1		15.53	+
PKS 2155–304 ⁵³	21 58 52.7	–30 13 18	HBL	0.116 ^{af}	97.10	89.8		87.20	+
BL Lacertae ⁵⁴	22 02 43.3	+42 16 40	IBL	0.069 ^x	14.15	365.6		51.73	+
B3 2247+381 ⁵⁵	22 50 06.6	+38 25 58	HBL	0.119 ^{ac}	10.60	42.3		4.48	+
RGB J2243+203 ⁵⁶	22 43 54.7	+20 21 04	HBL	Unknown	4.94	9.5		0.47	
1ES 2344+514 ⁵⁷	23 47 04.9	+51 42 17	HBL	0.044 ^t	20.38	143.9		29.33	+
H 2356–309 ⁵⁸	23 59 09.4	–30 37 22	HBL	0.165 ^{ag}	5.68	17.1		0.97	

TeV detection references:

¹H.E.S.S. Collaboration (2013a), ²Becherini et al. (2012), ³Aleksić et al. (2015), ⁴Mazin & MAGIC Collaboration (2012), ⁵Aharonian et al. (2008), ⁶Aliu et al. (2009), ⁷Aharonian et al. (2007a), ⁸H.E.S.S. Collaboration (2013c), ⁹Aleksić et al. (2010), ¹⁰Aliu et al. (2012), ¹¹Aharonian et al. (2007b), ¹²H.E.S.S. Collaboration. (2012), ¹³H.E.S.S. Collaboration (2013b), ¹⁴Wystan Benbow for the VERITAS (2011), ¹⁵Archambault et al. (2013), ¹⁶Aharonian et al. (2010), ¹⁷Aliu et al. (2011), ¹⁸De Lotto & Magic Collaboration (2012), ¹⁹Acciari et al. (2010b), ²⁰Anderhub et al. (2009), ²¹Acciari et al. (2009), ²²Mirzoyan (2014b), ²³H.E.S.S. Collaboration (2012), ²⁴Mirzoyan (2015), ²⁵Albert et al. (2007a), ²⁶Aharonian et al. (2007d), ²⁷Punch et al. (1992), ²⁸Albert et al. (2006b), ²⁹Mirzoyan (2014a), ³⁰Aleksić et al. (2012a), ³¹Albert et al. (2006a), ³²Acciari et al. (2008), ³³Cortina (2013b), ³⁴Aleksić et al. (2011), ³⁵Mukherjee (2015a), ³⁶Errando et al. (2008), ³⁷H.E.S.S. Collaboration (2013), ³⁸Acciari et al. (2010a), ³⁹Horan et al. (2002), ⁴⁰Ong (2010), ⁴¹Mukherjee (2015b), ⁴²H.E.S.S. Collaboration (2013), ⁴³H. E. S. S. Collaboration (2014), ⁴⁴Aharonian et al. (2006b), ⁴⁵Quinn et al. (1996), ⁴⁶Cortina (2013a), ⁴⁷Aleksić et al. (2014c), ⁴⁸Berger (2011), ⁴⁹H.E.S.S. Collaboration (2011a), ⁵⁰Nishiyama (1999), ⁵¹Mariotti (2010), ⁵²Aharonian et al. (2005), ⁵³Chadwick et al. (1999), ⁵⁴Albert et al. (2007b), ⁵⁵Aleksić et al. (2012b), ⁵⁶Holder (2014), ⁵⁷Catanese et al. (1998), ⁵⁸Aharonian et al. (2006a).

Redshift references:

^aJones et al. (2009), ^bPita et al. (2014), ^cSbarufatti et al. (2005), ^dRines et al. (2003), ^eFurniss et al. (2013), ^fWoo et al. (2005), ^gFalco et al. (1999), ^hDonato et al. (2001), ⁱLiu & Zhang (2002), ^jCraig & Fruscione (1997), ^kFalomo & Kotilainen (1999), ^lShaw et al. (2013), ^mPaturel et al. (2002), ⁿMassaro et al. (2009), ^oRector et al. (2003), ^pAbazajian et al. (2009), ^qGiommi et al. (2005), ^rSnellen et al. (2002), ^sAlbert et al. (2007c), ^tLavaux & Hudson (2011), ^uVillforth et al. (2009), ^vRines et al. (2003), ^wHealey et al. (2008), ^xVéron-Cetty & Véron (2010), ^yFey et al. (2004), ^zShaw et al. (2012), ^{aa}Aliu et al. (2014b), ^{ab}Urry et al. (2000), ^{ac}Laurent-Muehleisen et al. (1999), ^{ad}Cerruti (2011), ^{ae}Berger et al. (2011), ^{af}Ganguly et al. (2013), ^{ag}Colless et al. (2001).

Table 3. Fit parameters for the log-parabola fits. (1) The object name, (2) source of N_H value, (3)-(5) the α , β parameters and the normalization for the log-parabola fit defined in Sect. 3, (6) the reduced χ^2 value and the number of degrees of freedom.

Object	N_H	α	β	N_l $10^{-2} \text{ cm}^{-2} \text{ s}^{-1} \text{ keV}^{-1}$	$\chi^2_{red}/n_{d.o.f}$
(1)	(2)	(3)	(4)	(5)	(6)
1ES 0033+595	LAB	0.93±0.05	0.66±0.07	2.277±0.044	1.048/366
	DL	0.97±0.05	0.93±0.07	2.327±0.045	1.043/366
	Will	1.49±0.05	0.47±0.07	3.201±0.065	0.999/366
	free	1.60±0.16	0.36±0.15	3.443±0.338	1.001/365
RGB J0136+391	LAB	2.07±0.02	0.41±0.04	0.718±0.008	0.922/259
	DL	2.07±0.02	0.41±0.04	0.717±0.008	0.924/259
	Will	2.16±0.02	0.30±0.04	0.744±0.008	0.900/259
	free	2.47±0.10	-0.07±0.12	0.848±0.036	0.846/258
3C 66A	LAB	2.45±0.02	-0.19±0.04	0.136±0.002	0.989/261
	DL	2.53±0.02	-0.29±0.05	0.140±0.002	0.960/261
	Will	2.60±0.02	-0.37±0.04	0.143±0.002	0.943/261
	free	2.76±0.08	-0.57±0.10	0.153±0.005	0.929/260
1ES 0229+200	LAB	1.41±0.03	0.38±0.05	0.381±0.006	1.162/265
	DL	1.48±0.03	0.30±0.05	0.384±0.006	1.164/265
	Will	1.63±0.03	0.14±0.05	0.424±0.006	1.178/265
	free	1.40±0.12	0.39±0.14	0.379±0.022	1.166/264
PKS 0447-439	LAB	2.49±0.01	0.27±0.03	0.654±0.006	1.177/273
	DL	2.55±0.01	0.19±0.03	0.697±0.006	1.154/273
	Will	2.49±0.01	0.27±0.03	0.657±0.006	1.175/273
	free	2.61±0.04	0.10±0.07	0.683±0.011	1.151/272
1ES 0502+675	LAB	1.89±0.02	0.51±0.03	1.315±0.011	1.104/348
	DL	1.90±0.02	0.49±0.03	1.322±0.011	1.110/348
	Will	2.21±0.02	0.13±0.03	1.517±0.012	1.032/348
	free	2.28±0.08	0.06±0.10	1.564±0.060	1.033/347
PKS 0548-322	LAB	1.73±0.01	0.17±0.02	1.028±0.006	0.956/529
	DL	1.71±0.01	0.20±0.02	1.016±0.006	0.955/529
	Will	1.75±0.01	0.15±0.02	1.037±0.006	0.959/529
	free	1.70±0.04	0.21±0.04	1.015±0.016	0.957/528
1ES 0647+250	LAB	2.01±0.12	0.45±0.03	0.966±0.006	1.139/426
	DL	2.07±0.01	0.38±0.03	0.992±0.006	1.128/426
	Will	2.26±0.01	0.17±0.03	1.079±0.006	1.128/426
	free	2.16±0.06	0.27±0.05	1.035±0.003	1.125/425
S5 0716+714	LAB	2.07±0.01	-0.15±0.02	0.116±0.001	1.029/434
	DL	2.11±0.01	-0.20±0.02	0.230±0.002	1.024/434
	Will	2.10±0.01	-0.19±0.02	0.230±0.002	1.025/434
	free	2.12±0.04	-0.22±0.05	0.231±0.004	1.026/433
1ES 0806+524	LAB	2.37±0.01	0.29±0.03	0.414±0.003	0.994/284
	DL	2.39±0.01	0.27±0.03	0.418±0.003	0.990/284
	Will	2.42±0.01	0.23±0.03	0.422±0.004	0.985/284
	free	2.46±0.06	0.18±0.08	0.429±0.008	0.987/283
1ES 1011+496	LAB	2.25±0.01	0.24±0.02	0.938±0.006	1.268/360
	DL	2.24±0.01	0.24±0.02	0.937±0.006	1.269/360
	Will	2.25±0.01	0.23±0.02	0.938±0.006	1.267/360
	free	2.32±0.04	0.15±0.05	0.961±0.013	1.260/359
1ES 1101-232	LAB	2.02±0.02	0.11±0.04	1.910±0.022	1.034/269
	DL	2.03±0.02	0.10±0.04	1.916±0.022	1.035/269
	Will	2.11±0.02	0.23±0.04	1.987±0.023	1.053/269
	free	1.89±0.08	0.25±0.10	1.812±0.061	1.028/268

Table 3 – *continued*

	(1)	(2)	(3)	(4)	(5)	(6)
Mrk 180	LAB	2.09±0.01	0.25±0.03	0.849±0.006	1.012/339	
	DL	2.11±0.01	0.23±0.03	0.854±0.006	1.005/339	
	Will	2.10±0.01	0.25±0.03	0.850±0.006	1.011/339	
	free	2.21±0.04	0.11±0.06	0.885±0.015	0.992/338	
RX J1136.5+6737	LAB	1.65±0.02	0.23±0.04	0.417±0.005	1.041/271	
	DL	1.68±0.02	0.21±0.04	0.421±0.005	1.040/271	
	Will	1.66±0.02	0.23±0.04	0.418±0.004	1.041/271	
	free	1.71±0.08	0.17±0.10	0.427±0.014	1.043/270	
1ES 1218+304	LAB	2.04±0.02	0.13±0.04	0.927±0.001	1.198/287	
	DL	2.02±0.02	0.15±0.04	0.921±0.001	1.195/287	
	Will	2.05±0.02	0.12±0.04	0.930±0.001	1.199/287	
	free	1.96±0.06	0.22±0.08	0.902±0.022	1.196/286	
W Comae	LAB	2.44±0.01	-0.24±0.04	0.065±0.001	1.015/253	
	DL	2.43±0.01	-0.21±0.04	0.065±0.001	1.042/253	
	Will	2.45±0.01	-0.25±0.04	0.065±0.001	1.010/253	
	free	2.63±0.06	-0.48±0.08	0.070±0.002	0.968/252	
MS 1221.8+2452	LAB	2.18±0.02	0.39±0.04	0.395±0.005	1.143/240	
	DL	2.18±0.02	0.39±0.04	0.396±0.004	1.143/240	
	Will	2.19±0.02	0.38±0.04	0.397±0.005	1.139/240	
	free	2.38±0.07	0.13±0.10	0.426±0.012	1.110/239	
4C +21.35	LAB	1.87±0.01	-0.48±0.03	0.064±0.001	1.032/374	
	DL	1.88±0.01	-0.49±0.03	0.064±0.001	1.035/374	
	Will	1.88±0.01	-0.49±0.03	0.064±0.001	1.036/374	
	free	1.75±0.05	-0.35±0.06	0.061±0.001	1.018/373	
3C 279	LAB	1.48±0.01	0.16±0.02	0.245±0.001	1.108/607	
	DL	1.49±0.01	0.14±0.02	0.246±0.001	1.110/607	
	Will	1.49±0.01	0.14±0.02	0.246±0.001	1.108/607	
	free	1.45±0.03	0.19±0.04	0.242±0.003	1.108/606	
PKS 1424+240	LAB	2.48±0.01	0.34±0.03	0.261±0.002	1.081/267	
	DL	2.47±0.01	0.36±0.03	0.260±0.003	1.093/267	
	Will	2.51±0.01	0.30±0.03	0.264±0.002	1.059/267	
	free	2.76±0.05	-0.04±0.07	0.288±0.006	0.968/266	
H 1426+428	LAB	1.84±0.01	0.10±0.01	1.423±0.006	1.245/583	
	DL	1.86±0.01	0.18±0.01	1.434±0.006	1.246/583	
	Will	1.84±0.01	0.20±0.01	1.424±0.006	1.245/583	
	free	1.84±0.02	0.19±0.03	1.425±0.014	1.247/582	
PKS 1510-089	LAB	1.39±0.01	-0.10±0.02	0.107±0.001	1.046/660	
	DL	1.44±0.01	-0.15±0.02	0.110±0.001	1.061/660	
	Will	1.54±0.01	-0.24±0.02	0.115±0.001	1.103/660	
	free	1.28±0.04	0.01±0.04	0.101±0.002	1.033/659	
PG 1553+113	LAB	2.25±0.01	0.13±0.02	1.046±0.006	1.299/432	
	DL	2.25±0.01	0.13±0.02	1.046±0.006	1.298/432	
	Will	2.30±0.01	0.07±0.02	1.065±0.006	1.288/432	
	free	2.33±0.03	0.03±0.05	1.076±0.015	1.290/431	
1ES 1959+650	LAB	1.91±0.01	0.40±0.02	7.301±0.042	1.263/466	
	DL	1.94±0.01	0.36±0.02	7.400±0.042	1.230/466	
	Will	2.29±0.01	-0.01±0.02	8.669±0.049	1.331/466	
	free	2.00±0.05	0.30±0.06	7.586±0.177	1.260/465	

Table 3 – *continued*

	(1)	(2)	(3)	(4)	(5)	(6)
PKS 2005–489	LAB	2.47±0.01	–0.05±0.03	0.920±0.007	0.984/326	
	DL	2.55±0.01	–0.14±0.03	0.947±0.007	0.996/326	
	Will	2.53±0.01	–0.11±0.03	0.937±0.007	0.989/326	
	free	2.47±0.04	–0.04±0.06	0.919±0.016	0.987/325	
PKS 2155–304	LAB	2.38±0.02	0.23±0.05	3.834±0.050	1.151/208	
	DL	2.39±0.02	0.21±0.05	3.852±0.051	1.149/208	
	Will	2.38±0.02	0.22±0.05	3.844±0.051	1.150/208	
	free	2.45±0.07	0.13±0.11	3.926±0.106	1.151/207	
BL Lacertae	LAB	1.23±0.02	0.48±0.02	0.266±0.002	1.164/615	
	DL	1.40±0.02	0.31±0.02	0.292±0.002	1.122/615	
	Will	1.82±0.02	–0.10±0.02	0.369±0.002	1.146/615	
	free	1.55±0.06	0.16±0.06	0.318±0.010	1.111/614	
B3 2247+381	LAB	2.03±0.02	0.52±0.04	0.375±0.004	1.036/282	
	DL	2.15±0.02	0.36±0.04	0.396±0.004	1.021/282	
	Will	2.35±0.02	0.13±0.04	0.433±0.004	1.023/282	
	free	2.24±0.10	0.27±0.12	0.411±0.019	1.022/281	
1ES 2344+514	LAB	1.86±0.01	0.29±0.01	0.528±0.003	1.080/531	
	DL	1.96±0.01	0.18±0.02	0.552±0.003	1.093/531	
	Will	2.40±0.01	–0.26±0.02	0.685±0.004	1.308/531	
	free	1.81±0.05	0.33±0.06	0.514±0.013	1.080/530	

Table 6. The summary of time-resolved spectral analysis. The table summarize the spectral parameters for the broken power-law fit to *Swift*/XRT data for the selected blazars. The time intervals are shown in Fig.8-12, while the corresponding spectral fits are presented in Fig. 13. The following columns show: (1) the name of the object, (2) the selected interval, (3) the normalization, (4)-(5) the spectral indices, (6) the break energy (7) the value of reduced χ^2 and the number of degree of freedom. The fits included in this Table are plotted in Fig. 13.

Object	Interval	N_b $10^{-3} \text{ cm}^{-2} \text{ s}^{-1} \text{ keV}^{-1}$	Γ_1	Γ_2	E_b keV	$\chi^2_{red}/n.d.o.f$
(1)	(2)	(3)	(4)	(5)	(6)	(7)
3C 66A	A	1.173±0.023	2.420±0.042	2.142±0.044	1.37±0.21	0.998/219
3C 66A	B	3.158±0.052	2.653±0.029	1.4±1.8	5.2±1.8	0.883/139
3C 66A	C	2.62±0.41	1.2±1.8	2.50±0.33	0.46±0.11	0.861/136
S5 0716+714	A	1.767±0.072	2.911±0.071	2.052±0.073	1.18±0.11	0.976/107
S5 0716+714	B	2.285±0.028	2.511±0.024	2.035±0.030	1.361±0.083	0.925/310
S5 0716+714	C	2.220±0.029	2.258±0.025	1.932±0.018	1.153±0.079	1.009/408
S5 0716+714	D	1.872±0.098	2.122±0.090	1.976±0.037	0.92±0.39	0.841/188
W Comae	A	0.855±0.079	2.550±0.016	1.84±0.20	4.07±0.46	0.956/163
W Comae	B	0.263±0.014	2.18±0.10	1.738±0.067	1.18±0.23	0.814/298
4C +21.35	A	0.556±0.015	2.071±0.054	1.437±0.032	1.180±0.087	0.835/253
4C +21.35	B	0.393±0.028	1.71±0.13	1.366±0.038	0.97±0.22	1.125/136
4C +21.35	C	0.915±0.025	2.340±0.052	1.454±0.036	1.209±0.063	0.877/230
BL Lacertae	A	3.132±0.035	2.346±0.039	1.941±0.014	1.237±0.062	1.129/523
BL Lacertae	B	4.176±0.080	1.947±0.066	1.703±0.012	1.10±0.12	1.143/533
BL Lacertae	C	2.245±0.053	2.111±0.078	1.782±0.016	1.10±0.11	0.936/430

ACKNOWLEDGEMENTS

A.W. acknowledges support by Polish Ministry of Science and Higher Education in Mobility Plus Program and Polish National Science Center for supporting this work through grant DEC–2011/03/N/ST9/01867. Support from the German Ministry for Education and Research (BMBF) through the Verbundforschung Astroteilchenphysik grant 05A11VH2 is gratefully acknowledged. This research was supported in part by PLGrid Infrastructure.

REFERENCES

- Abazajian K. N. et al., 2009, *ApJS*, 182, 543
 Abdo A. A. et al., 2010, *ApJ*, 716, 30
 Acciari V. et al., 2009, *ApJ*, 690, L126
 Acciari V. A. et al., 2010a, *ApJ*, 708, L100
 Acciari V. A. et al., 2010b, *ApJ*, 715, L49
 Acciari V. A. et al., 2011, *ApJ*, 738, 169
 Acciari V. A. et al., 2008, *ApJ*, 684, L73
 Aharonian F. et al., 2010, *A&A*, 521, A69
 Aharonian F. et al., 2009, *ApJ*, 696, L150
 Aharonian F. et al., 2005, *A&A*, 436, L17
 Aharonian F. et al., 2007a, *A&A*, 475, L9
 Aharonian F. et al., 2007b, *A&A*, 473, L25
 Aharonian F. et al., 2008, *A&A*, 481, L103
 Aharonian F. et al., 2007c, *ApJ*, 664, L71
 Aharonian F. et al., 2006a, *A&A*, 455, 461
 Aharonian F. et al., 2006b, *A&A*, 448, L19
 Aharonian F. et al., 2007d, *A&A*, 470, 475
 Aharonian F. A., 2000, *New A*, 5, 377
 Albert J. et al., 2006a, *ApJ*, 642, L119
 Albert J. et al., 2006b, *ApJ*, 648, L105
 Albert J. et al., 2007a, *ApJ*, 667, L21
 Albert J. et al., 2007b, *ApJ*, 666, L17
 Albert J. et al., 2007c, *ApJ*, 667, L21
 Aleksić J. et al., 2012a, *A&A*, 544, A142
 Aleksić J. et al., 2012b, *A&A*, 539, A118
 Aleksić J. et al., 2014a, *A&A*, 567, A135
 Aleksić J. et al., 2015, *MNRAS*, 446, 217
 Aleksić J. et al., 2014b, *ArXiv e-prints*: 1408.1975
 Aleksić J. et al., 2014c, *A&A*, 563, A90
 Aleksić J. et al., 2013, *A&A*, 556, A67
 Aleksić J. et al., 2014d, *A&A*, 563, A91
 Aleksić J. et al., 2010, *ApJ*, 723, L207
 Aleksić J. et al., 2011, *ApJ*, 730, L8
 Aliu E. et al., 2009, *ApJ*, 692, L29
 Aliu E. et al., 2014a, *ApJ*, 797, 89
 Aliu E. et al., 2013, *ApJ*, 775, 3
 Aliu E. et al., 2012, *ApJ*, 750, 94
 Aliu E. et al., 2014b, *ArXiv e-prints*: 1411.1439
 Aliu E. et al., 2011, *ApJ*, 742, 127
 Anderhub H. et al., 2009, *ApJ*, 704, L129
 Archambault S. et al., 2013, *ApJ*, 776, 69
 Arnal E. M., Bajaja E., Larrarte J. J., Morras R., Pöppel W. G. L., 2000, *A&AS*, 142, 35
 Arnaud K. A., 1996, in *Astronomical Society of the Pacific Conference Series*, Vol. 101, *Astronomical Data Analysis Software and Systems V*, Jacoby G. H., Barnes J., eds., p. 17
 Atoyan A. M., Dermer C. D., 2003, *ApJ*, 586, 79
 Bajaja E., Arnal E. M., Larrarte J. J., Morras R., Pöppel W. G. L., Kalberla P. M. W., 2005, *A&A*, 440, 767
 Barthelmy S. D. et al., 2005, *Space Sci. Rev.*, 120, 143
 Baumgartner W. H., Tueller J., Markwardt C. B., Skinner G. K., Barthelmy S., Mushotzky R. F., Evans P. A., Gehrels N., 2013, *ApJS*, 207, 19
 Becherini Y., Boisson C., Cerruti M., H. E. S. S. Collaboration, 2012, in *American Institute of Physics Conference Series*, Vol. 1505, *American Institute of Physics Conference Series*, Aharonian F. A., Hofmann W., Rieger F. M., eds., pp. 490–493
 Begelman M. C., Blandford R. D., Rees M. J., 1984, *Reviews of Modern Physics*, 56, 255
 Berger K., 2011, *International Cosmic Ray Conference*, 8, 169
 Berger K., Giavitto G., Lindfors E., Takalo L., Paneque D., Stamerra A., On behalf of the MAGIC Collaboration, 2011, *ArXiv e-prints*, 1110.6368
 Bevington P., Robinson D., 2003, *Data reduction and error analysis for the physical sciences*, McGraw-Hill Higher Education. McGraw-Hill
 Böttcher M. et al., 2010, *ApJ*, 725, 2344
 Böttcher M., Reimer A., Sweeney K., Prakash A., 2013, *ApJ*, 768, 54
 Brinkmann W., Papadakis I. E., Raeth C., Mimica P., Haberl F., 2005, *A&A*, 443, 397
 Burrows D. N. et al., 2005, *Space Sci. Rev.*, 120, 165
 Cappi M., Comastri A., Molendi S., Palumbo G. G. C., Della Ceca R., Maccacaro T., 1994, *MNRAS*, 271, 438
 Catanese M. et al., 1998, *ApJ*, 501, 616
 Cerruti M., 2011, *International Cosmic Ray Conference*, 8, 109
 Chadwick P. M. et al., 1999, *ApJ*, 513, 161
 Chiappetti L. et al., 1999, *ApJ*, 521, 552
 Colless M. et al., 2001, *MNRAS*, 328, 1039
 Cortina J., 2013a, *The Astronomer’s Telegram*, 5080, 1
 Cortina J., 2013b, *The Astronomer’s Telegram*, 5038, 1
 Craig N., Fruscione A., 1997, *AJ*, 114, 1356
 Dame T. M., Hartmann D., Thaddeus P., 2001, *ApJ*, 547, 792
 De Lotto B., Magic Collaboration, 2012, *Journal of Physics Conference Series*, 375, 052021
 Dermer C. D., Schlickeiser R., Mastichiadis A., 1992, *A&A*, 256, L27
 Dickey J. M., Lockman F. J., 1990, *ARA&A*, 28, 215
 Donato D., Ghisellini G., Tagliaferri G., Fossati G., 2001, *A&A*, 375, 739
 Donato D., Sambruna R. M., Gliozzi M., 2005, *A&A*, 433, 1163
 Edelson R. A., Krolik J. H., 1988, *ApJ*, 333, 646
 Errando M. et al., 2008, in *American Institute of Physics Conference Series*, Vol. 1085, *American Institute of Physics Conference Series*, Aharonian F. A., Hofmann W., Rieger F., eds., pp. 423–426
 Evans P. A. et al., 2009, *MNRAS*, 397, 1177
 Falco E. E. et al., 1999, *PASP*, 111, 438
 Falomo R., Kotilainen J. K., 1999, *A&A*, 352, 85
 Ferrero E., Wagner S. J., Emmanoulopoulos D., Ostorero L., 2006, *A&A*, 457, 133
 Fey A. L. et al., 2004, *AJ*, 127, 3587
 Foschini L. et al., 2006, *A&A*, 455, 871
 Fossati G. et al., 2000, *ApJ*, 541, 153

- Fossati G., Maraschi L., Celotti A., Comastri A., Ghisellini G., 1998, *MNRAS*, 299, 433
- Furniss A., Fumagalli M., Danforth C., Williams D. A., Prochaska J. X., 2013, *ApJ*, 766, 35
- Ganguly R. et al., 2013, *MNRAS*, 435, 1233
- Gaur H., 2014, *Journal of Astrophysics and Astronomy*
- Gehrels N. et al., 2004, *ApJ*, 611, 1005
- Giommi P., Capalbi M., Fiocchi M., Memola E., Perri M., Piranomonte S., Rebecchi S., Massaro E., 2002, in *Blazar Astrophysics with BeppoSAX and Other Observatories*, Giommi P., Massaro E., Palumbo G., eds., p. 63
- Giommi P. et al., 1999, *A&A*, 351, 59
- Giommi P., Padovani P., Perlman E., 2000, *MNRAS*, 317, 743
- Giommi P., Piranomonte S., Perri M., Padovani P., 2005, *A&A*, 434, 385
- Gopal-Krishna, Goyal A., Joshi S., Karthick C., Sagar R., Wiita P. J., Anupama G. C., Sahu D. K., 2011, *MNRAS*, 416, 101
- H. E. S. S. Collaboration, 2014, *ArXiv e-prints*, 1410.5897
- Hartmann D., Burton W. B., 1997, *Atlas of Galactic Neutral Hydrogen*
- Healey S. E. et al., 2008, *ApJS*, 175, 97
- H.E.S.S. Collaboration, 2010, *A&A*, 511, A52
- H.E.S.S. Collaboration, 2011a, *A&A*, 529, A49
- H.E.S.S. Collaboration, 2011b, *A&A*, 533, A110
- H.E.S.S. Collaboration, 2012, *A&A*, 539, A149
- H.E.S.S. Collaboration., 2012, *A&A*, 538, A103
- H.E.S.S. Collaboration, 2012, *A&A*, 542, A94
- H.E.S.S. Collaboration, 2013a, *A&A*, 554, A72
- H.E.S.S. Collaboration, 2013b, *A&A*, 552, A118
- H.E.S.S. Collaboration, 2013c, *A&A*, 559, A136
- H.E.S.S. Collaboration, 2013, *MNRAS*, 434, 1889
- H.E.S.S. Collaboration, 2013, *A&A*, 554, A107
- H.E.S.S. Collaboration, 2014, *A&A*, 571, A39
- Holder J., 2014, *The Astronomer's Telegram*, 6849, 1
- Horan D. et al., 2002, *ApJ*, 571, 753
- Inoue S., Takahara F., 1996, *ApJ*, 463, 555
- Jones D. H. et al., 2009, *MNRAS*, 399, 683
- Kadler M., Eisenacher D., Ros E., Mannheim K., Elsässer D., Bach U., 2012, *A&A*, 538, L1
- Kalberla P. M. W., Burton W. B., Hartmann D., Arnal E. M., Bajaja E., Morras R., Pöppel W. G. L., 2005, *A&A*, 440, 775
- Kapanadze B., Romano P., Vercellone S., Kapanadze S., 2014, *MNRAS*, 444, 1077
- Kirk J. G., Rieger F. M., Mastichiadis A., 1998, *A&A*, 333, 452
- Kubo H., Takahashi T., Madejski G., Tashiro M., Makino F., Inoue S., Takahara F., 1998, *ApJ*, 504, 693
- Landau R. et al., 1986, *ApJ*, 308, 78
- Laurent-Muehleisen S. A., Kollgaard R. I., Feigelson E. D., Brinkmann W., Siebert J., 1999, *ApJ*, 525, 127
- Lavaux G., Hudson M. J., 2011, *MNRAS*, 416, 2840
- Leahy J. P., 1991, *Interpretation of large scale extragalactic jets*, Hughes P. A., ed., p. 100
- Liao N. H., Bai J. M., 2015, *New A*, 34, 134
- Liu F. K., Zhang Y. H., 2002, *A&A*, 381, 757
- Maraschi L., Ghisellini G., Celotti A., 1992, *ApJ*, 397, L5
- Mariotti M., 2010, *The Astronomer's Telegram*, 2753, 1
- Marquardt D. W., 1963, *SIAM Journal on Applied Mathematics*, 11, 431
- Massaro E., Giommi P., Leto C., Marchegiani P., Maselli A., Perri M., Piranomonte S., Sclavi S., 2009, *A&A*, 495, 691
- Massaro E., Perri M., Giommi P., Nesci R., 2004a, *A&A*, 413, 489
- Massaro E., Perri M., Giommi P., Nesci R., Verrecchia F., 2004b, *A&A*, 422, 103
- Massaro E., Tramacere A., Perri M., Giommi P., Tosti G., 2006, *A&A*, 448, 861
- Massaro F., Tramacere A., Cavaliere A., Perri M., Giommi P., 2008, *A&A*, 478, 395
- Mazin D., MAGIC Collaboration, 2012, in *American Institute of Physics Conference Series*, Vol. 1505, American Institute of Physics Conference Series, Aharonian F. A., Hofmann W., Rieger F. M., eds., pp. 186–193
- Meyer E. T., Fossati G., Georganopoulos M., Lister M. L., 2011, *ApJ*, 740, 98
- Mirzoyan R., 2014a, *The Astronomer's Telegram*, 6062, 1
- Mirzoyan R., 2014b, *The Astronomer's Telegram*, 5768, 1
- Mirzoyan R., 2015, *The Astronomer's Telegram*, 7080, 1
- Mücke A., Protheroe R. J., Engel R., Rachen J. P., Stanev T., 2003, *Astroparticle Physics*, 18, 593
- Mukherjee R., 2015a, *The Astronomer's Telegram*, 7516, 1
- Mukherjee R., 2015b, *The Astronomer's Telegram*, 7433, 1
- Nishiyama T., 1999, *International Cosmic Ray Conference*, 3, 370
- Ong R. A., 2010, *The Astronomer's Telegram*, 2786, 1
- Padovani P., Costamante L., Giommi P., Ghisellini G., Celotti A., Wolter A., 2004, *MNRAS*, 347, 1282
- Padovani P. et al., 2001, *MNRAS*, 328, 931
- Padovani P., Giommi P., 1995, *ApJ*, 444, 567
- Paturel G., Dubois P., Petit C., Woelfel F., 2002, *LEDA*
- Perlman E. S. et al., 2005, *ApJ*, 625, 727
- Perlman E. S., Madejski G., Stocke J. T., Rector T. A., 1999, *ApJ*, 523, L11
- Perlman E. S., Stocke J. T., Wang Q. D., Morris S. L., 1996, *ApJ*, 456, 451
- Petropoulou M., Mastichiadis A., 2015, *MNRAS*, 447, 36
- Pian E. et al., 1998, *ApJ*, 492, L17
- Pita S. et al., 2014, *A&A*, 565, A12
- Punch M. et al., 1992, *Nature*, 358, 477
- Quinn J. et al., 1996, *ApJ*, 456, L83
- Raiteri C. M. et al., 2009, *A&A*, 507, 769
- Raiteri C. M., Villata M., Kadler M., Krichbaum T. P., Böttcher M., Fuhrmann L., Orío M., 2006, *A&A*, 452, 845
- Ravasio M. et al., 2002, *A&A*, 383, 763
- Ravasio M., Tagliaferri G., Ghisellini G., Tavecchio F., 2004, *A&A*, 424, 841
- Rector T. A., Perlman E., Sambruna R., Madejski G., Rantakyro F., CANGAROO Collaboration, 2002, *PASA*, 19, 158
- Rector T. A., Gabuzda D. C., Stocke J. T., 2003, *AJ*, 125, 1060
- Reinthal R. et al., 2012, *Journal of Physics Conference Series*, 355, 012017
- Rines K., Geller M. J., Kurtz M. J., Diaferio A., 2003, *AJ*, 126, 2152
- Roming P. W. A. et al., 2005, *Space Sci. Rev.*, 120, 95
- Saito S., Stawarz L., Tanaka Y. T., Takahashi T., Madejski G., D'Ammando F., 2013, *ApJ*, 766, L11
- Sambruna R. M., Barr P., Giommi P., Maraschi L., Tagli-

- aferri G., Treves A., 1994, *ApJS*, 95, 371
- Sambruna R. M., Maraschi L., Urry C. M., 1996, *ApJ*, 463, 444
- Sambruna R. M., Urry C. M., Ghisellini G., Maraschi L., 1995, *ApJ*, 449, 567
- Sbarufatti B., Treves A., Falomo R., 2005, *ApJ*, 635, 173
- Schlegel D. J., Finkbeiner D. P., Davis M., 1998, *ApJ*, 500, 525
- Sembay S., Edelson R., Markowitz A., Griffiths R. G., Turner M. J. L., 2002, *ApJ*, 574, 634
- Sembay S., Warwick R. S., Urry C. M., Sokoloski J., George I. M., Makino F., Ohashi T., Tashiro M., 1993, *ApJ*, 404, 112
- Shaw M. S. et al., 2012, *ApJ*, 748, 49
- Shaw M. S. et al., 2013, *ApJ*, 764, 135
- Sikora M., Begelman M. C., Rees M. J., 1994, *ApJ*, 421, 153
- Snellen I. A. G., McMahon R. G., Hook I. M., Browne I. W. A., 2002, *MNRAS*, 329, 700
- Tagliaferri G. et al., 2001, *A&A*, 368, 38
- Tagliaferri G. et al., 2000, *A&A*, 354, 431
- Tagliaferri G. et al., 2003, *A&A*, 400, 477
- Takahashi T. et al., 1996, *ApJ*, 470, L89
- Tanihata C. et al., 2000, *ApJ*, 543, 124
- Tavecchio F., Maraschi L., Ghisellini G., 1998, *ApJ*, 509, 608
- Tramacere A. et al., 2007, *A&A*, 467, 501
- Urry C. M., Sambruna R. M., Worrall D. M., Kollgaard R. I., Feigelson E. D., Perlman E. S., Stocke J. T., 1996, *ApJ*, 463, 424
- Urry C. M., Scarpa R., O'Dowd M., Falomo R., Pesce J. E., Treves A., 2000, *ApJ*, 532, 816
- Vaughan S., Edelson R., Warwick R. S., Uttley P., 2003, *MNRAS*, 345, 1271
- Vercellone S. et al., 2011, *ApJ*, 736, L38
- Véron-Cetty M.-P., Véron P., 2010, *A&A*, 518, A10
- Villforth C., Nilsson K., Østensen R., Heidt J., Niemi S.-M., Pförr J., 2009, *MNRAS*, 397, 1893
- Wagner S., 2009, in *Astrophysics with All-Sky X-Ray Observations*, Kawai N., Mihara T., Kohama M., Suzuki M., eds., p. 186
- Wagner S. J., Witzel A., 1995, *ARA&A*, 33, 163
- Wierzcholska A., Siejkowski H., 2015, *MNRAS*, 452, L11
- Willingale R., Starling R. L. C., Beardmore A. P., Tanvir N. R., O'Brien P. T., 2013, *MNRAS*, 431, 394
- Wolter A. et al., 1998, *A&A*, 335, 899
- Woo J.-H., Urry C. M., van der Marel R. P., Lira P., Maza J., 2005, *ApJ*, 631, 762
- Worrall D. M., Wilkes B. J., 1990, *ApJ*, 360, 396
- Wystan Benbow for the VERITAS, 2011, *ArXiv e-prints*, 1110.0040
- Xue Y., Yuan F., Cui W., 2006, *ApJ*, 647, 194
- Zhang Y. H., 2008, *ApJ*, 682, 789
- Zhang Y. H. et al., 1999, *ApJ*, 527, 719
- Zhang Y. H. et al., 2002, *ApJ*, 572, 762
- Zhang Y. H., Treves A., Celotti A., Qin Y. P., Bai J. M., 2005, *ApJ*, 629, 686
- Zhang Y. H., Treves A., Maraschi L., Bai J. M., Liu F. K., 2006, *ApJ*, 637, 699

Online material for: X-ray spectral studies of TeV γ -ray emitting blazars

Alicja Wierzcholska^{1,2*}, Stefan J. Wagner¹

¹*Landessternwarte, Universität Heidelberg, Königstuhl 12, D 69117 Heidelberg, Germany*

²*Institute of Nuclear Physics, Polish Academy of Sciences, ul. Radzikowskiego 152, 31-342 Kraków, Poland*

27 January 2016

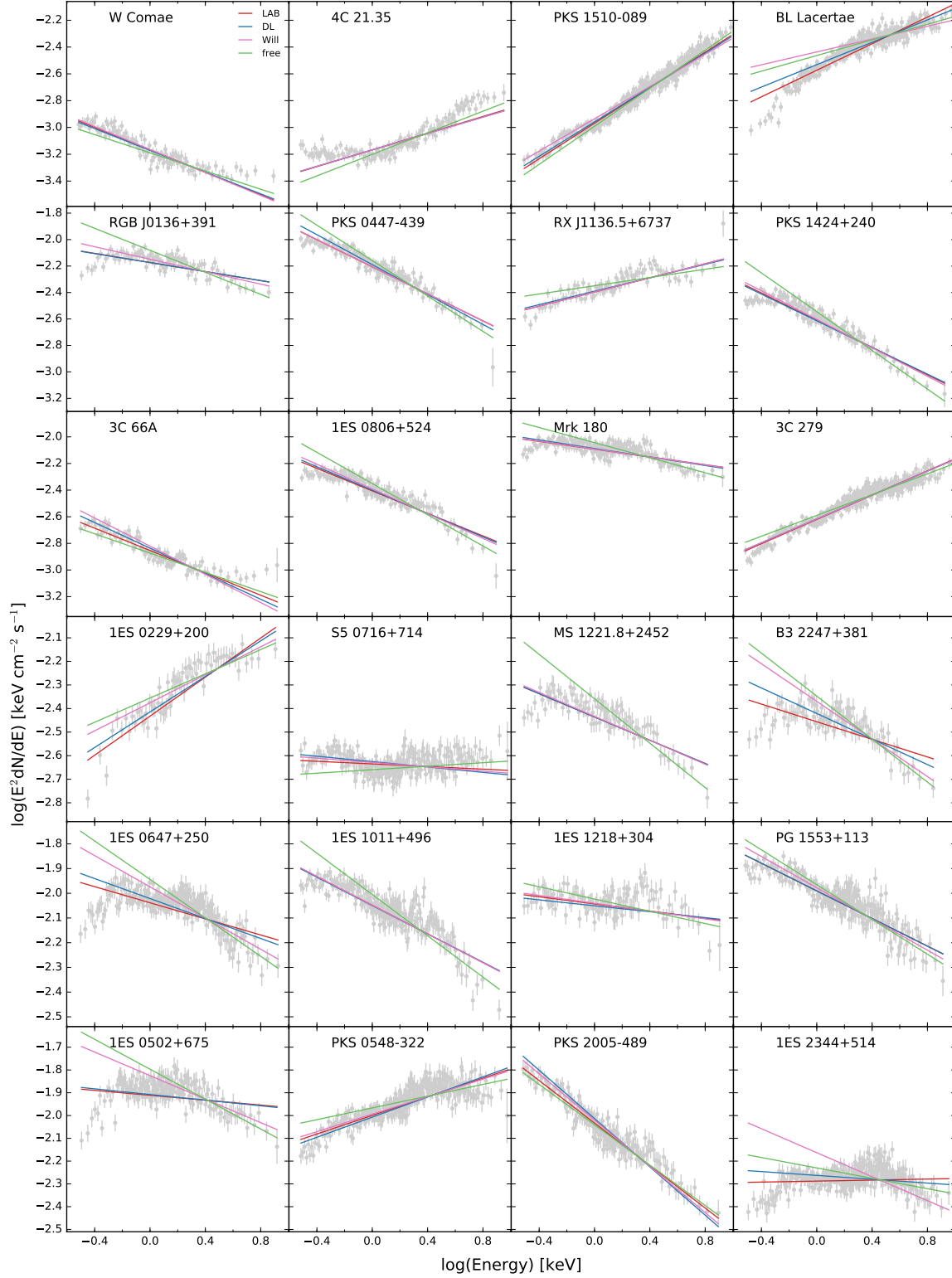


Figure 2. The X-ray spectral energy distributions of 29 selected blazars sorted by increasing flux density. The names of the sources are given in the upper part of each panel. Four power-law models using different values of N_H are presented using different colours: red – N_H taken from the LAB survey (Kalberla et al. 2005), blue – N_H value taken from Dickey & Lockman (1990), magenta – N_H value taken from Willingale et al. (2013) and green – free N_H value. Data (grey points) presented in the figure are those fitted with the power-law model with the Galactic absorption value taken from LAB survey.

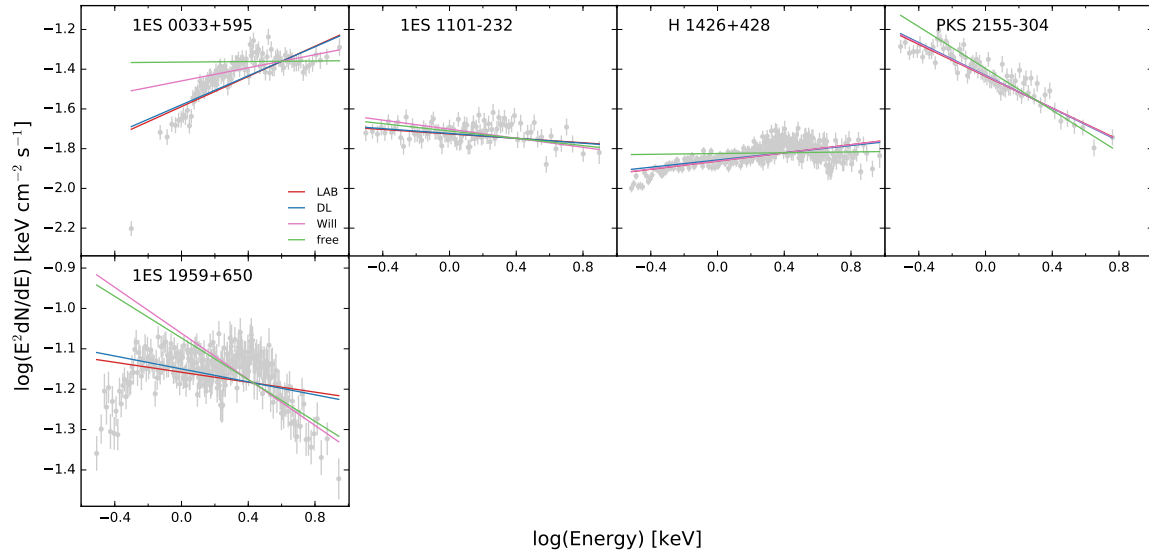


Figure 2 – continued

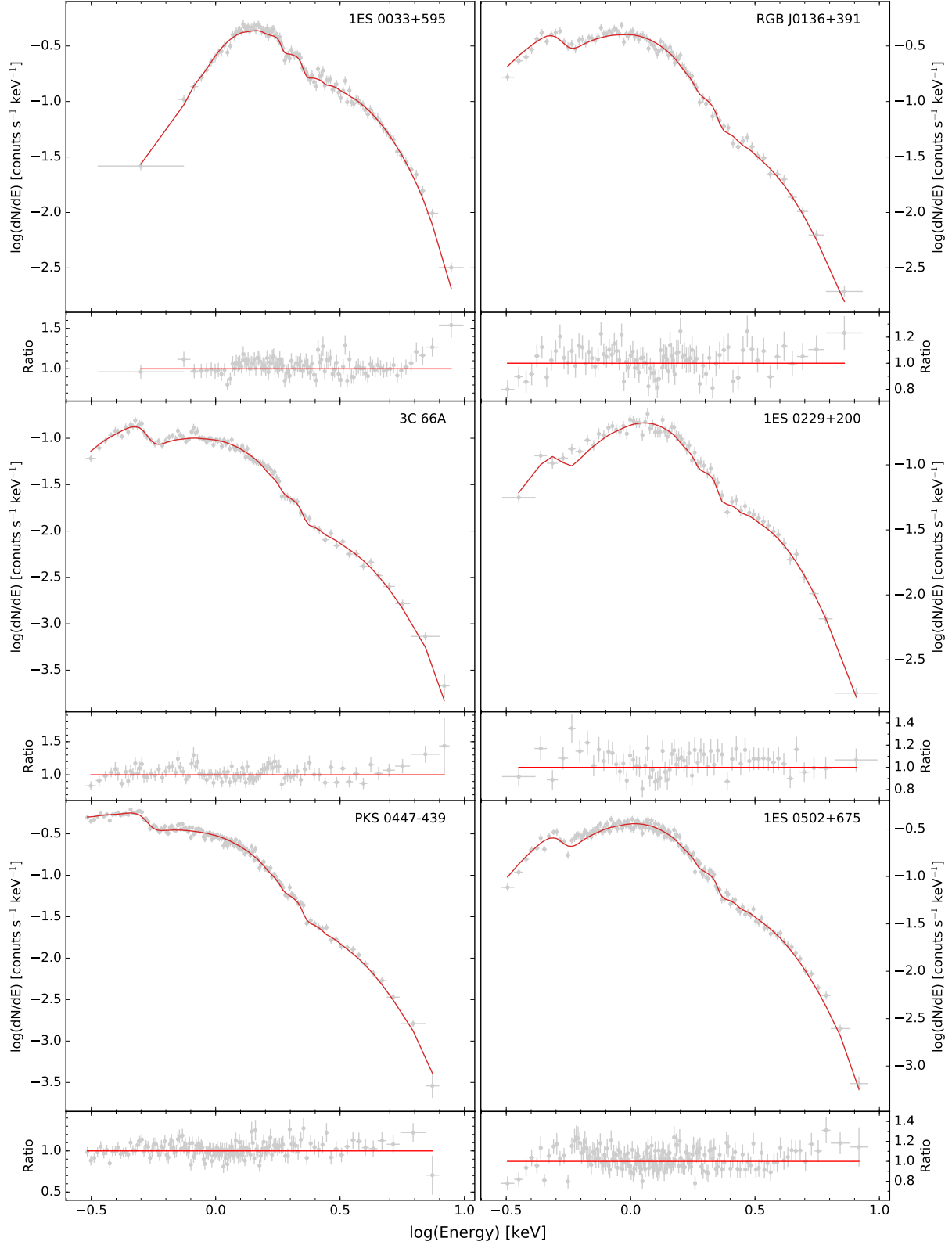


Figure 3. The X-ray spectra fitted with the log-parabola model with the Galactic absorption value taken from LAB survey and the ratios (data points divided by the folded model). The plots present spectra for: 1ES 0033+595, RGB J0136+391, 3C 66A, 1ES 0229+200, PKS 0447-437, 1ES 0502+675. The name of each object is also given in the upper right corner of each plot.

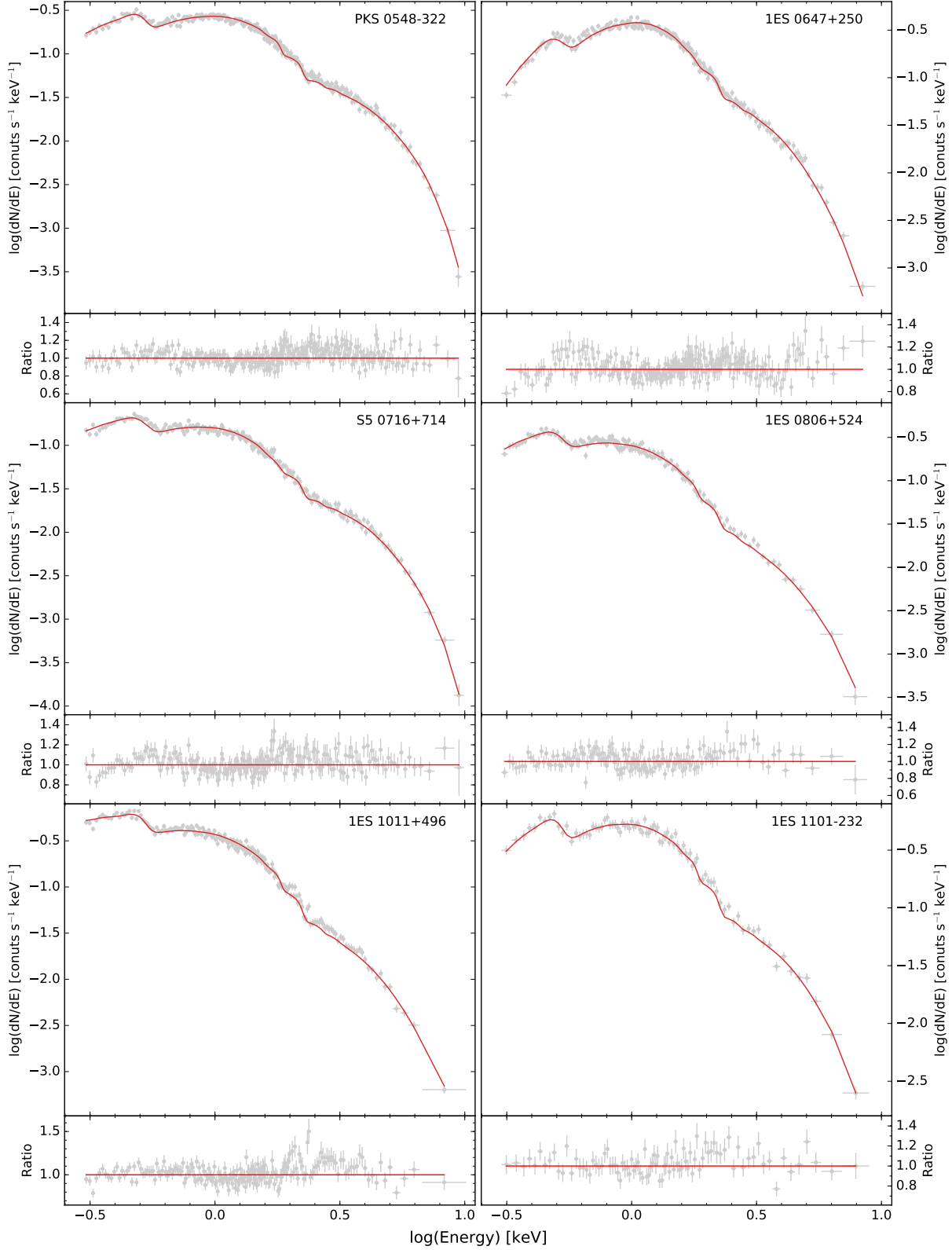


Figure 4. The X-ray spectra fitted with the log-parabola model with the Galactic absorption value taken from LAB survey and the ratios (data points divided by the folded model). The following plots present spectra for: PKS 0548-322, 1ES 0647+250, S5 0716+714, 1ES 0806+524, 1ES 1011+496, 1ES 1101-232. The name of each object is also given in the upper right corner of each plot.

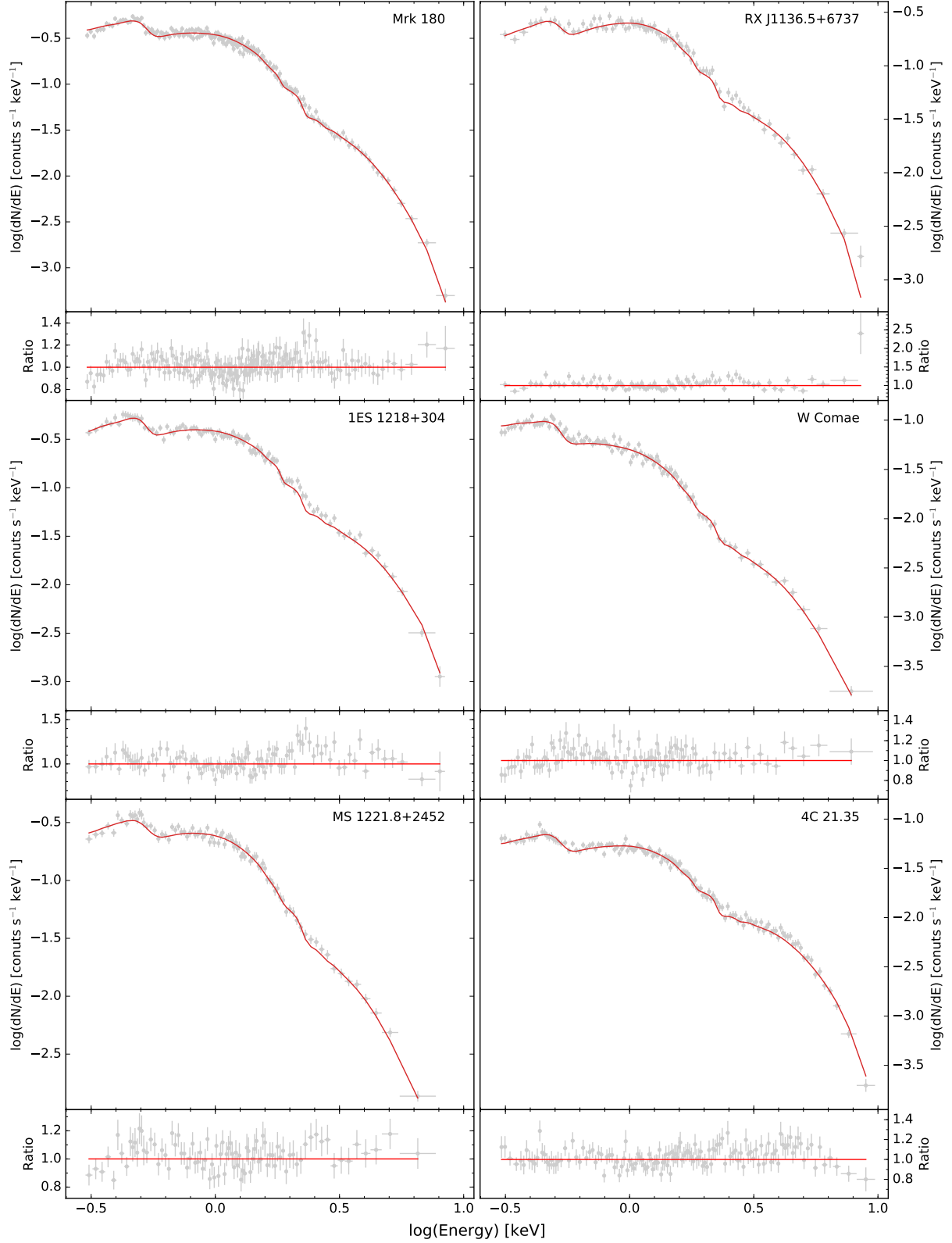


Figure 5. The X-ray spectra fitted with the log-parabola model with the Galactic absorption value taken from LAB survey and the ratios (data points divided by the folded model). The following plots present spectra for: Mrk 180, RX J1136.5+6737, 1ES 1218+304, W Comae, MS 1221.8+2452, 4C 21.35. The name of each object is also given in the upper right corner of each plot.

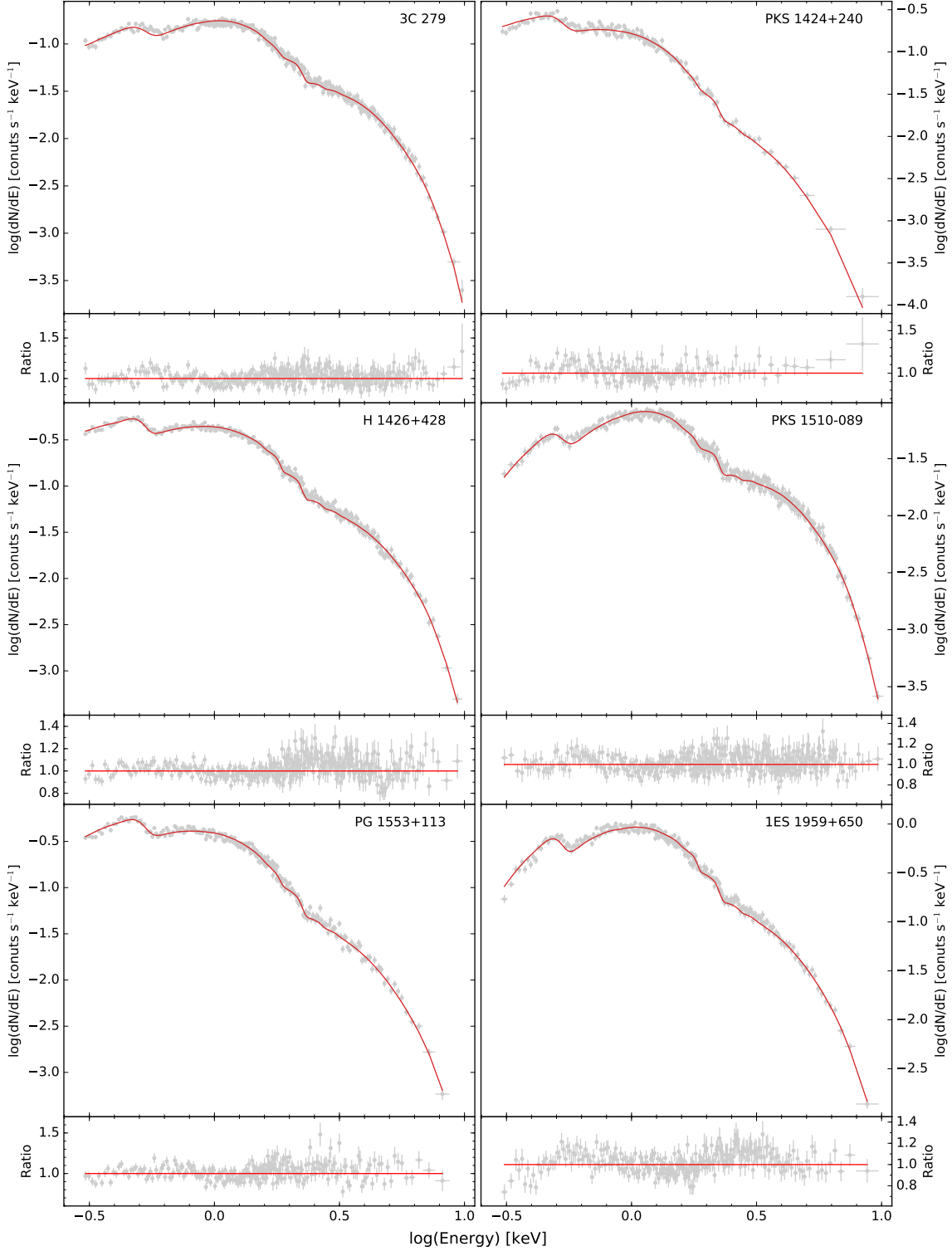


Figure 6. The X-ray spectra fitted with the log-parabola model with the Galactic absorption value taken from LAB survey and the ratios (data points divided by the folded model). The following plots present spectra for: 3C 279, PKS 1424+240, H 1426+428, PKS 1510-089, PG 1553+113, 1ES 1959+650. The name of each object is also given in the upper right corner of each plot.

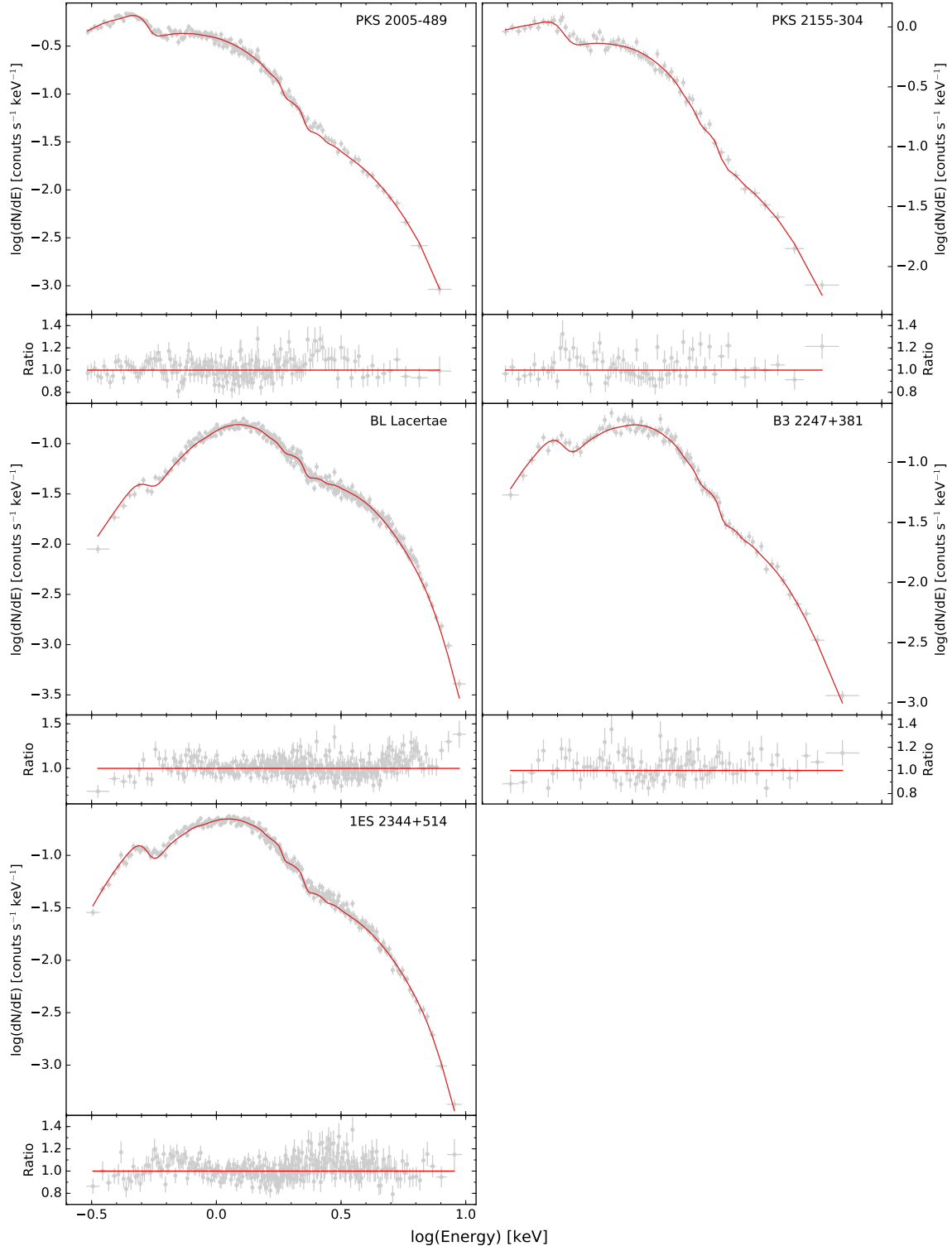


Figure 7. The X-ray spectra fitted with the log-parabola model with the Galactic absorption value taken from LAB survey and the ratios (data points divided by the folded model). The following plots present spectra for: PKS 2005-489, PKS 2155-304, BL Lacertae, B3 2247+381, 1ES 2344+514. The name of each object is also given in the upper right corner of each plot.

Table 2. The comparison of Galactic column density values. (1) The object name, (2)-(5) the N_H values provided by Kalberla et al. (2005), Dickey & Lockman (1990), Willingale et al. (2013), respectively, (6)-(8) the free N_H value obtained with the log-parabola, the power-law and the broken power-law model fitted.

Object	N_H^{LAB} [10^{20} cm $^{-2}$]	N_H^{DL} [10^{20} cm $^{-2}$]	N_H^{H2} [10^{20} cm $^{-2}$]	N_H^{Will} [10^{20} cm $^{-2}$]	$N_H^{LP,free}$ [10^{20} cm $^{-2}$]	$N_H^{PL,free}$ [10^{20} cm $^{-2}$]	$N_H^{BP,free}$ [10^{20} cm $^{-2}$]
(1)	(2)	(3)	(4)	(5)	(6)	(7)	(8)
SHBL J001355.9–185406	2.13	2.09	0.17	2.30			
KUV 00311–1938	1.67	1.59	0.10	1.77			
1ES 0033+595	41.80	42.70	14.40	56.20	59.36±0.42	68.80±0.19	
RGB J0136+391	6.00	5.96	1.30	7.30	12.0±1.5	11.10±0.53	
RGB J0152+017	2.68	2.89	0.23	2.91			
3C 66A	7.37	8.49	2.02	9.40	11.79±0.12	6.31±0.42	7.50±0.54
1ES 0229+200	8.06	9.20	3.69	11.80	7.86±1.98	13.19±0.81	
PKS 0301–243	1.70	1.82	0.10	1.79			
IC 310	12.20	13.30	6.16	18.30			
RBS 0413	8.84	10.50	4.11	12.90			
1ES 0347–121	3.09	3.60	0.56	3.65			
1ES 0414+009	8.85	10.30	4.88	13.70			
PKS 0447–439	1.18	1.99	0.04	1.22	2.79±0.58	3.57±0.27	
1ES 0502+675	9.37	9.56	5.16	14.50	15.61±1.35	16.37±0.46	
VER J0521+211	28.60	33.40	14.40	42.90			
PKS 0548–322	2.58	2.18	0.30	2.87	2.14±0.50	4.41±0.22	
RX J0648.7+1516	16.80	19.40	8.72	25.50			
1ES 0647+250	11.80	12.80	4.06	15.80	14.30±1.00	17.82±0.35	
RGB J0710+591	4.48	5.57	0.75	5.23			
S5 0716+714	3.22	3.82	0.39	3.60	3.96±0.54	1.92±0.22	6.04±0.66
1ES 0806+524	4.16	4.45	0.73	4.89	5.45±0.78	7.11±0.34	
RBS 0723	3.39	4.06	0.41	3.79			
1RXS J101015.9–311909	7.90	7.36	2.33	10.20			
S4 0954+65	4.80	3.69	1.50	6.30			
1ES 1011+496	0.84	0.79	0.02	0.86	1.75±0.47	3.04±0.22	
1ES 1101–232	5.51	5.63	1.39	6.90	3.67±1.12	6.36±0.49	
Markarian 421	1.91	1.43	0.11	2.01			
Markarian 180	1.17	1.42	0.05	1.22	2.71±0.58	3.67±0.26	
RX J1136.5+6737	1.03	1.33	0.03	1.06	1.8±1.1	3.57±0.47	
1ES 1215+303	1.70	1.68	0.09	1.80			
1ES 1218+304	1.99	1.75	0.13	2.12	1.00±0.80	3.05±0.37	
W Comae	2.04	1.84	0.14	2.18	4.54±0.74	8.75±0.32	2.54±0.50
MS 1221.8+2452	1.79	1.80	1.78	1.91	4.55±0.98	5.73±0.43	
4C +21.35	2.12	2.26	0.17	2.29	0.48±0.64	0.00±0.00	1.07±0.73
S3 1227+25	1.42	1.54	0.08	1.50			
3C 279	2.01	2.21	0.21	2.22	1.58±0.44	3.74±0.20	
1ES 1312–423	7.77	7.93	3.42	11.20			
PKS 1424+240	2.84	2.67	0.35	3.19	6.63±0.74	6.25±0.32	
H 1426+428	1.11	1.38	0.04	1.14	1.17±0.33	3.12±0.15	
1ES 1440+122	1.58	1.61	0.14	1.72			
PKS 1441+25	3.12	2.68	0.37	3.49			
PKS 1510–089	6.99	7.80	2.46	9.45	5.09±0.60	5.28±0.25	
AP Librae	8.36	8.70	4.25	4.17			
PG 1553+113	3.67	3.69	0.68	4.35	4.71±0.46	5.03±0.20	
Markarian 501	1.58	1.67	0.08	1.66			
H 1722+119	8.70	8.61	5.09	13.80			
1ES 1727+502	2.38	2.79	0.23	2.60			
1ES 1741+196	7.32	6.82	2.26	9.58			
HESS J1943+213	82.40	88.10	14.40	96.80			
1ES 1959+650	9.83	10.30	6.06	15.90	11.17±0.80	15.11±0.31	
MAGIC J2001+435	37.00	43.10	14.40	51.40			
PKS 2005–489	3.94	5.04	0.72	4.66	3.91±0.57	3.54±0.25	
PKS 2155–304	1.52	1.71	0.11	1.63	2.47±0.94	3.51±0.43	
BL Lacertae	18.30	21.60	12.00	30.30	24.77±1.16	27.59±0.46	25.09±1.02
B3 2247+381	10.20	12.20	5.16	15.40	13.5±1.6	16.87±0.59	
RGB J2243+203	5.25	5.41	1.07	6.33			
1ES 2344+514	15.10	16.80	9.47	24.60	14.34±0.88	19.18±0.33	
H 2356–309	1.42	1.32	0.06	1.48			

Table 4. Fit parameters for the power-law fits. (1) The object name, (2) source of N_H value, (3)-(4) the spectral index and the normalization for the power-law fit defined in Sect. 3, (5) the reduced χ^2 value and the number of degrees of freedom, (6) the test statistics value for F-test, (7) probability, (8) preferred spectral model: PO - for the power-law and LP - for the log-parabola model.

Object	N_H	Γ	N_p $10^{-2} \text{ cm}^{-2} \text{ s}^{-1} \text{ keV}^{-1}$	$\chi^2_{red}/n_{d.o.f}$	F	p-value	Model
(1)	(2)	(3)	(4)	(5)	(6)	(7)	(8)
1ES 0033+595	LAB	1.62±0.01	2.581±0.037	1.800/367	264	1·10 ⁻¹⁶	LP
	DL	1.64±0.01	2.635±0.038	1.736/367	244	1·10 ⁻¹⁶	LP
	Will	1.84±0.02	3.476±0.052	1.143/367	53	1·10 ⁻¹²	LP
	free	1.99±0.03	4.322±0.151	1.013/366	5	0.02	PO
RGB J0136+391	LAB	2.17±0.01	0.671±0.006	1.321/260	114	1·10 ⁻¹⁶	LP
	DL	2.17±0.01	0.670±0.006	1.329/260	115	1·10 ⁻¹⁶	LP
	Will	2.23±0.01	0.711±0.007	1.094/260	57	1·10 ⁻¹³	LP
	free	2.42±0.03	0.830±0.018	0.845/259	0.7	0.4	PO
3C 66A	LAB	2.42±0.02	0.140±0.001	1.066/262	21	6·10 ⁻⁶	LP
	DL	2.48±0.02	0.146±0.001	1.137/262	49	2·10 ⁻¹¹	LP
	Will	2.53±0.02	0.151±0.001	1.223/262	78	1·10 ⁻¹⁶	LP
	free	2.36±0.03	0.134±0.003	1.047/261	34	1·10 ⁻⁸	LP
1ES 0229+200	LAB	1.59±0.02	0.370±0.005	1.381/266	51	8·10 ⁻¹²	LP
	DL	1.62±0.02	0.385±0.005	1.300/266	32	4·10 ⁻⁸	LP
	Will	1.70±0.02	0.421±0.006	1.202/266	6	0.01	PO
	free	1.74±0.03	0.441±0.013	1.194/265	7	7·10 ⁻³	LP
PKS 0447-439	LAB	2.51±0.01	0.623±0.004	1.474/274	70	3·10 ⁻¹⁵	LP
	DL	2.57±0.01	0.647±0.004	1.285/274	32	4·10 ⁻⁸	LP
	Will	2.51±0.01	0.624±0.004	1.462/274	67	7·10 ⁻¹⁵	LP
	free	2.67±0.02	0.694±0.009	1.155/273	2	0.2	PO
1ES 0502+675	LAB	2.05±0.01	1.227±0.009	1.885/349	247	1·10 ⁻¹⁶	LP
	DL	2.06±0.01	1.237±0.009	1.833/349	228	1·10 ⁻¹⁶	LP
	Will	2.26±0.01	1.497±0.011	1.079/349	17	5·10 ⁻⁵	LP
	free	2.33±0.02	1.597±0.028	1.031/348	1	0.6	PO
PKS 0548-322	LAB	1.80±0.01	1.001±0.005	1.142/530	104	1·10 ⁻¹⁶	LP
	DL	1.78±0.01	0.984±0.005	1.216/530	146	1·10 ⁻¹⁶	LP
	Will	1.81±0.01	1.014±0.005	1.098/530	78	1·10 ⁻¹⁶	LP
	free	1.87±0.01	1.080±0.011	1.000/529	25	9·10 ⁻⁷	LP
1ES 0647+250	LAB	1.16±0.01	0.915±0.005	2.013/427	328	1·10 ⁻¹⁶	LP
	DL	2.20±0.01	0.952±0.005	1.729/427	228	1·10 ⁻¹⁶	LP
	Will	2.32±0.01	1.062±0.006	1.236/427	42	3·10 ⁻¹⁰	LP
	free	2.39±0.02	1.138±0.015	1.155/426	12	5·10 ⁻⁴	LP
S5 0716+714	LAB	2.03±0.01	0.232±0.001	1.145/435	50	6·10 ⁻¹²	LP
	DL	2.06±0.01	0.237±0.001	1.228/435	88	1·10 ⁻¹⁶	LP
	Will	2.05±0.01	0.235±0.001	1.195/435	73	2·10 ⁻¹⁶	LP
	free	1.96±0.01	0.219±0.002	1.069/434	19	1·10 ⁻⁵	LP
1ES 0806+524	LAB	2.42±0.01	0.393±0.003	1.316/285	93	1·10 ⁻¹⁶	LP
	DL	2.44±0.01	0.398±0.003	1.252/285	76	2·10 ⁻¹⁶	LP
	Will	2.46±0.01	0.406±0.003	1.171/285	55	2·10 ⁻¹²	LP
	free	2.59±0.02	0.446±0.007	1.003/284	6	0.02	PO
1ES 1011+496	LAB	2.29±0.01	0.895±0.005	1.606/361	97	1·10 ⁻¹⁶	LP
	DL	2.29±0.01	0.892±0.005	1.622/361	101	1·10 ⁻¹⁶	LP
	Will	2.29±0.01	0.895±0.005	1.600/361	96	1·10 ⁻¹⁶	LP
	free	2.42±0.02	0.989±0.011	1.282/360	7	7·10 ⁻³	LP
1ES 1101-232	LAB	2.06±0.01	1.880±0.019	1.057/270	7	9·10 ⁻³	LP
	DL	2.06±0.01	1.890±0.019	1.054/270	6	0.01	PO
	Will	2.11±0.02	1.986±0.020	1.049/270	-0.1	1	PO
	free	2.09±0.03	1.945±0.042	1.049/269	6	0.01	PO

Table 4 – *continued*

	(1)	(2)	(3)	(4)	(5)	(6)	(7)	(8)
Mrk 180	LAB	2.15±0.01	0.808±0.005	1.326/240	-24	1	PO	
	DL	2.16±0.01	0.818±0.005	1.259/340	87	1·10 ⁻¹⁶	LP	
	Will	2.15±0.01	0.810±0.005	1.312/340	102	1·10 ⁻¹⁶	LP	
	free	2.28±0.02	0.905±0.011	0.999/339	3	0.07	PO	
RX J1136.5+6737	LAB	1.73±0.01	0.401±0.004	1.171/272	35	1·10 ⁻⁸	LP	
	DL	1.75±0.01	0.407±0.004	1.141/272	27	3·10 ⁻⁷	LP	
	Will	1.73±0.01	0.402±0.004	1.168/272	34	1·10 ⁻⁸	LP	
	free	1.84±0.03	0.448±0.010	1.050/271	3	0.1	PO	
1ES 1218+304	LAB	2.07±0.01	0.906±0.008	1.248/288	13	4·10 ⁻⁴	LP	
	DL	2.06±0.01	0.896±0.008	1.264/288	18	4·10 ⁻⁵	LP	
	Will	2.08±0.01	0.911±0.008	1.240/288	11	1·10 ⁻³	LP	
	free	2.12±0.02	0.948±0.017	1.220/287	7	0.01	LP	
W Comae	LAB	2.42±0.01	0.068±0.001	1.160/254	37	4·10 ⁻⁹	LP	
	DL	2.41±0.01	0.067±0.001	1.144/254	26	7·10 ⁻⁷	LP	
	Will	2.43±0.01	0.068±0.001	1.172/254	42	5·10 ⁻¹⁰	LP	
	free	2.34±0.03	0.065±0.001	1.113/253	39	2·10 ⁻⁹	LP	
MS 1221.8+2452	LAB	2.25±0.01	0.366±0.005	1.563/241	90	1·10 ⁻¹⁶	LP	
	DL	2.25±0.01	0.367±0.003	1.561/241	89	1·10 ⁻¹⁶	LP	
	Will	2.25±0.01	0.368±0.003	1.533/241	84	1·10 ⁻¹⁶	LP	
	free	2.47±0.03	0.438±0.009	1.112/240	1	0.2	PO	
4C +21.35	LAB	1.69±0.01	0.068±0.001	1.763/375	267	1·10 ⁻¹⁶	LP	
	DL	1.69±0.01	0.068±0.001	1.795/375	276	1·10 ⁻¹⁶	LP	
	Will	1.70±0.01	0.068±0.001	1.802/375	278	1·10 ⁻¹⁶	LP	
	free	1.60±0.02	0.063±0.001	1.349/374	123	1·10 ⁻¹⁶	LP	
3C 279	LAB	1.54±0.01	0.240±0.001	1.293/608	102	1·10 ⁻¹⁶	LP	
	DL	1.55±0.01	0.242±0.001	1.260/608	83	1·10 ⁻¹⁶	LP	
	Will	1.55±0.01	0.242±0.001	1.259/608	84	1·10 ⁻¹⁶	LP	
	free	1.61±0.01	0.257±0.002	1.152/607	25	7·10 ⁻⁷	LP	
H 1426+428	LAB	1.90±0.01	1.373±0.005	1.678/584	204	1·10 ⁻¹⁶	LP	
	DL	1.91±0.01	1.390±0.005	1.583/584	159	1·10 ⁻¹⁶	LP	
	Will	1.90±0.01	1.374±0.005	1.667/584	199	1·10 ⁻¹⁶	LP	
	free	1.99±0.01	1.498±0.011	1.317/583	34	1·10 ⁻⁸	LP	
PKS 1424+240	LAB	2.52±0.01	0.245±0.002	1.498/268	104	1·10 ⁻¹⁶	LP	
	DL	2.50±0.01	0.243±0.002	1.560/268	116	1·10 ⁻¹⁶	LP	
	Will	2.54±0.01	0.250±0.002	1.384/268	83	1·10 ⁻¹⁶	LP	
	free	2.73±0.02	0.285±0.004	0.966/267	0.4	0.5	PO	
PKS 1510–089	LAB	1.34±0.01	0.107±0.001	1.096/661	33	1·10 ⁻⁸	LP	
	DL	1.36±0.01	0.110±0.001	1.168/661	68	1·10 ⁻¹⁵	LP	
	Will	1.40±0.01	0.116±0.001	1.379/661	166	1·10 ⁻¹⁶	LP	
	free	1.29±0.01	0.102±0.001	1.032/660	0.4	0.5	PO	
PG 1553+113	LAB	2.28±0.01	1.023±0.004	1.405/433	36	40·10 ⁻⁹	LP	
	DL	2.28±0.01	1.023±0.004	1.402/433	36	5·10 ⁻⁹	LP	
	Will	2.32±0.01	1.053±0.005	1.314/433	10	2·10 ⁻³	LP	
	free	2.35±0.01	1.084±0.010	1.288/432	0.3	0.6	PO	
1ES 1959+650	LAB	2.06±0.01	6.950±0.036	2.116/467	316	1·10 ⁻¹⁶	LP	
	DL	2.08±0.01	7.082±0.037	1.967/467	281	1·10 ⁻¹⁶	LP	
	Will	2.29±0.01	8.676±0.046	1.329/467	0.3	0.6	PO	
	free	2.26±0.01	8.448±0.100	1.317/466	22	3·10 ⁻⁶	LP	

Table 4 – *continued*

(1)	(2)	(3)	(4)	(5)	(6)	(7)	(8)
PKS 2005–489	LAB	2.47±0.01	0.927±0.006	0.990/327	3	0.1	PO
	DL	2.53±0.01	0.970±0.006	1.083/327	30	1·10 ⁻⁷	LP
	Will	2.51±0.01	0.955±0.006	1.040/327	18	3·10 ⁻⁵	LP
	free	2.44±0.02	0.911±0.011	0.986/326	0.7	0.4	PO
PKS 2155–304	LAB	2.40±0.02	3.671±0.037	1.261/209	21	9·10 ⁻⁶	LP
	DL	2.41±0.02	3.704±0.037	1.239/209	17	4·10 ⁻⁵	LP
	Will	2.41±0.02	3.690±0.037	1.248/209	19	2·10 ⁻⁵	LP
	free	2.53±0.03	4.013±0.085	1.153/208	1	0.2	PO
BL Lacertae	LAB	1.50±0.01	0.267±0.002	2.002/616	444	1·10 ⁻¹⁶	LP
	DL	1.58±0.01	0.294±0.002	1.452/616	182	1·10 ⁻¹⁶	LP
	Will	1.76±0.01	0.366±0.002	1.172/616	15	1·10 ⁻⁴	LP
	free	1.71±0.01	0.344±0.004	1.121/615	6	0.01	PO
B3 2247+381	LAB	2.19±0.01	0.350±0.005	1.632/283	164	1·10 ⁻¹⁶	LP
	DL	2.27±0.01	0.379±0.003	1.304/283	79	1·10 ⁻¹⁶	LP
	Will	2.40±0.01	0.427±0.004	1.055/283	10	1·10 ⁻³	LP
	free	2.46±0.03	0.449±0.010	1.035/282	5	0.03	PO
1ES 2344+514	LAB	1.99±0.01	0.515±0.003	1.473/532	195	1·10 ⁻¹⁶	LP
	DL	2.04±0.01	0.546±0.003	1.247/532	76	1·10 ⁻¹⁶	LP
	Will	2.26±0.01	0.687±0.004	1.572/532	108	1·10 ⁻¹⁶	LP
	free	2.11±0.01	0.589±0.007	1.142/531	31	3·10 ⁻⁸	LP

Table 5. Fit parameters for the broken power-law fits. (1) The object name, (2) source of N_H value, (3)-(6) the spectral indices, normalization and break energy for the broken power-law fit defined in Sect. 3, (7) the reduced χ^2 value and the number of degrees of freedom.

Object	N_H	Γ_1	Γ_2	N_b $10^{-2} \text{ cm}^{-2} \text{ s}^{-1} \text{ keV}^{-1}$	E_b keV	$\chi^2_{red}/n.d.o.f$
(1)	(2)	(3)	(4)	(5)	(6)	(7)
3C 66A	LAB	2.462±0.017	1.746±0.170	0.139±0.001	3.383±0.328	0.949/260
	DL	2.540±0.018	1.794±0.140	0.145±0.001	3.064±0.261	0.961/260
	Will	2.615±0.020	1.936±0.104	0.150±0.001	2.568±0.213	0.985/260
	free	2.470±0.040	1.739±0.168	0.140±0.001	3.372±0.340	0.952/259
S5 0716+714	LAB	2.168±0.024	1.937±0.016	0.221±0.003	1.094±0.100	0.986/433
	DL	2.240±0.026	1.942±0.015	0.223±0.003	1.087±0.075	0.967/433
	Will	2.213±0.025	1.940±0.015	0.223±0.003	1.092±0.082	0.973/433
	free	2.511±0.085	1.965±0.017	0.231±0.002	1.046±0.042	0.942/432
W Comae	LAB	2.492±0.019	2.076±0.074	0.066±0.001	2.027±0.234	0.988/252
	DL	2.474±0.018	2.080±0.076	0.066±0.001	2.047±0.252	0.993/252
	Will	2.504±0.019	2.070±0.071	0.669±0.001	2.028±0.218	0.986/252
	free	2.538±0.050	2.071±0.069	0.677±0.001	1.976±0.212	0.987/251
4C +21.35	LAB	2.106±0.034	1.442±0.021	0.061±0.001	1.183±0.054	0.989/373
	DL	2.124±0.034	1.444±0.021	0.062±0.001	1.177±0.052	0.990/373
	Will	2.128±0.034	1.444±0.021	0.616±0.001	1.176±0.052	0.991/373
	free	1.978±0.093	1.432±0.022	0.604±0.001	1.222±0.071	0.987/372
BL Lacertae	LAB	1.155±0.023	1.705±0.014	0.260±0.002	1.611±0.048	1.173/614
	DL	1.374±0.021	1.728±0.016	0.286±0.002	1.766±0.081	1.122/614
	Will	1.996±0.047	1.727±0.010	0.363±0.005	1.095±0.087	1.098/614
	free	1.570±0.056	1.740±0.019	0.318±0.010	1.983±0.232	1.105/613

REFERENCES

- Dickey J. M., Lockman F. J., 1990, *ARA&A*, 28, 215
Kalberla P. M. W., Burton W. B., Hartmann D., Arnal
E. M., Bajaja E., Morras R., Pöppel W. G. L., 2005, *A&A*,
440, 775
Willingale R., Starling R. L. C., Beardmore A. P., Tanvir
N. R., O'Brien P. T., 2013, *MNRAS*, 431, 394